SINGLE-SHOT OPTICAL PROBING OF LASER-GENERATED PLASMAS

-Master Thesis-

For obtaining the academic degree
Master of Science (M.Sc.)

Abbe School of Photonics

Friedrich-Schiller-Universität Jena

Prepared and Submitted by: -

Faran Irshad

Project Supervisor:

Prof. Dr. Malte C. Kaluza

Dr. Sebastian Keppler

Table of Contents

1 Introduction

Lasers have captured scientific interest since their inception and increasing the on-target intensity has resulted in powerful petawatt (≈10^{15}W) laser systems across the globe [1]. Such a laser gives the possibility to study and optimize processes such as electron [2] or ion [3] acceleration resulting from interaction of extreme electric fields (E ≥ 0.5 TV/m) with matter [4]. An important future application of ion acceleration has been cancer therapy, since ions can offer certain medical advantages over conventional radiation sources (electrons or photon sources) [5]. Target normal sheath acceleration (TNSA) is an ion acceleration mechanism that gives rise to energetic ion beams when an intense laser pulse interacts with thin (several micrometers) solid targets. One of the important steps in this process is a pre-plasma created by intense pre-pulses, amplified spontaneous emission or the rising edge of the main pulse, which although less intense than the main pulse, is nevertheless sufficient to ionize the front surface of target [6]. Thus, the main pulse interacts with the pre-formed plasma that can greatly impact the laser-absorption processes. The effect of these pre-plasma properties on the TNSA process is currently under investigation using the POLARIS laser system in Jena, Germany.

The pre-plasma formed due to pre-pulses can result in a complex interplay of laser absorption processes. Several absorption processes such as resonance absorption, vacuum heating, normal skin effect, anomalous skin effect can play a significant role concerning the absorption of the laser into the target. This can then have an impact on the final energy of the ion beams resulting from TNSA. Thus, controlling the pre-plasma properties to generate higher energy and higher beam-quality ion beams is essential. A higher energy and better beam-quality of the ions from TNSA can act as an alternative comparatively compact ion sources as opposed to the large conventional ion accelerators.

A complete system with a pump pulse and a probe laser pulse has been developed at POLARIS in Jena to probe the laser-plasma interactions and map the evolution of the plasma over time. A regenerative amplifier serves as the source for both the pump pulse and the probe pulse. The pump pulse generates the plasmas when it is focused on a target material. A series of pulses

separated in time are generated and used to temporally probe the plasma dynamics in a single shot. The focus of the thesis is to use this single-shot probing system and fully characterize laser-generated plasmas from aluminum targets in terms of plasma electron density scale lengths and plasma electron temperatures under various pump pulse intensities and polarization states.

The thesis starts with a discussion of fundamental theoretical concepts in chapter 2 of laser beams and moves on to describe the mechanisms with which, the plasma is created. A brief overview of TNSA process then follows with a subsequent explanation of the different absorption processes. In chapter 3, the experimental setup, including the target geometries that were used to generate and probe the plasma is discussed in detail. Chapter 4 outlines the analysis procedure and theory used to calculate the electron density from the interferograms. It also gives an example analysis of the interferogram that results in the plasma scale length and plasma electron temperature. After that in the final chapter, the detailed results for both linear and circular polarizations are presented and discussed.

2 Fundamental Concepts

This chapter discusses the theoretical concepts used during the work of this master's thesis starting from a mathematical description of ultrashort pulses. Understanding the theory of ultrashort pulses is important to generate a series of probe pulses starting from a single pulse. Moving on the chapter discusses the basics of Gaussian beam optics, after which the spatial and temporal coherence of these ultrashort pulses is discussed. The focus is then shifted to the different mechanisms of plasma creation and the plasma parameters used in this thesis to characterize the plasma. This work is motivated by the desire to optimize the TNSA process, so the fundamentals of this process and the contributing absorption physics is then outlined.

2.1 Spatio-Temporal Characteristics of Ultrashort Pulses

2.1.1 Mathematical Description

A simple laser pulse can be understood as a multiplication of two functions. The first function shown in Figure 1a) is an oscillating sinusoidal term representing the electromagnetic field with its wave vector $\vec{k}$ and the angular carrier frequency ω_o and the second shown in Figure 1b) is an envelope function which determines the shape and duration of the laser pulse [7]. Figure 1c) represents the laser pulse, which here contains a high number of oscillations inside the envelope. For this thesis, the electromagnetic pulse has an oscillating frequency of $291\mathrm{THz}$ or a wavelength of $1.03\mu\mathrm{m}$. An ultrashort pulse has the same form as described above but the duration of the envelope function is less than 1 picosecond and thus it has fewer oscillations under the envelope

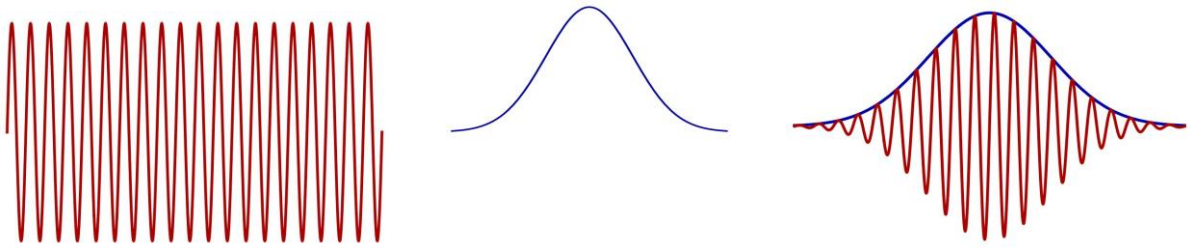

a) b) c)

Figure 1: A visual representation of multiplying an a) oscillating electromagnetic wave with an b) envelope to result in c) a Laser pulse.

for a fixed carrier frequency ω_o. Mathematically the above laser pulse propagating in z can be written in analytic representation as [8]

$$E(t,z) = A(t,z)\exp\{i(k_z z - \omega_o t)\} + c.c, \tag{1}$$

where $A(t,\vec{r})$ is the envelope function that determines the shape of the pulse as well as the duration. This laser pulse can be converted into the frequency domain using Fourier transformation [9]

$$\bar{E}(\omega,z) = \frac{1}{2\pi}\int_{-\infty}^{+\infty} E(t,z)\exp(i\omega t)\,dt, \tag{2}$$

where $\bar{E}(\omega,z)$ is the complete representation of the pulse in frequency domain. This complex quantity can be represented in the standard exponential form as [7]

$$\bar{E}(\omega,z) = \sqrt{S(\omega)}e^{i\phi(\omega)}, \tag{3}$$

where $S(\omega)$ is the spectral density, which denotes the amplitude of each of the frequency components of the ultrashort pulse and $\phi(\omega)$ is the spectral phase, which denotes the relative position of each of the frequency components with respect to each other. Using Fourier analysis on a gaussian function, a fundamental result of waves known as the time bandwidth product can be derived. For a gaussian beam this product is $\Delta\omega\Delta t = 4\ln 2$, where $\Delta\omega$ is the bandwidth of the pulse and Δt is the pulse duration. As a direct result of the time bandwidth product, a larger bandwidth implies a shorter pulse duration but for the generation of the ultrashort pulses the spectral phases also need to be in-phase or in more popular terms mode-locked [10].

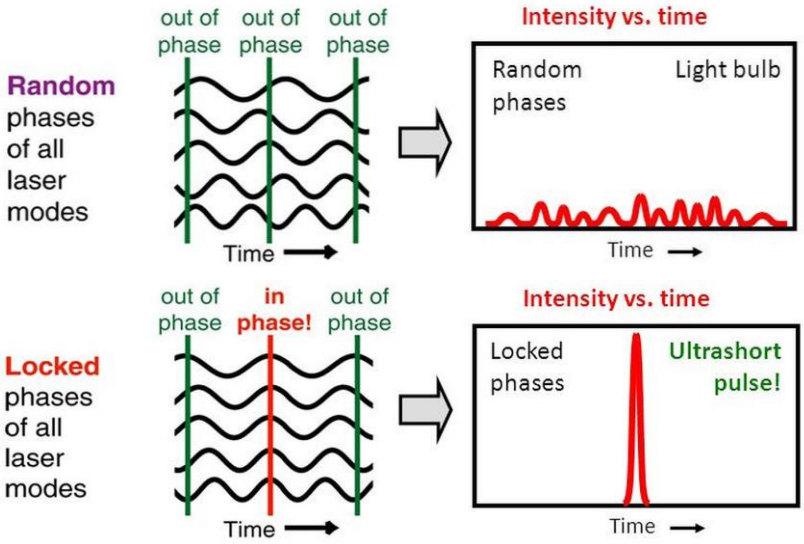

Figure 2: An ultrashort pulse is a consequence of locking the phases of all the frequency components or modes of the laser [10].

Figure 2 shows the concept of locking all the phases of frequency components of a laser more commonly known as longitudinal modes or simply modes. If the modes of the laser have random phases, then random intensity fluctuations result instead of an ultrashort pulse.

2.1.2 Gaussian Beam Optics

In this section, the relevant spatial characteristics of the ultrashort pulses described in the previous section is outlined. These laser beams have a high degree of directionality, meaning

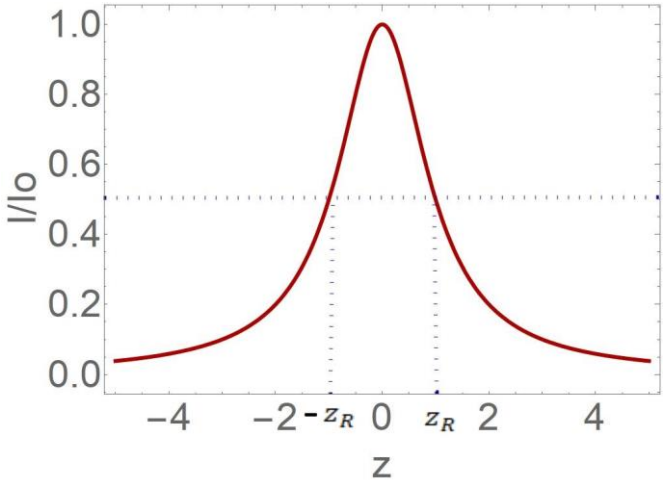

Figure 3: The peak intensity of the Gaussian beam on axis $I(r = 0, z)$ as a function of the propagation distance.

that the optical power of the light wave is mostly concentrated in a spatially confined area [11]. In this work, the transverse profile of the optical intensity of these beams can be represented by a gaussian function as [12]

$$I(r,z) = I_o \left[\frac{w_o}{w(z)}\right]^2 \exp\left\{-(4\ln 2)\left(\frac{r}{w(z)}\right)^2\right\}, \quad (4)$$

where w_o is the Full Width Half Maximum (FWHM) of the beam at the point of focus (z=0) known as the waist. The width of the gaussian beam also changes as the beam propagates and is given as [13]

$$w(z) = w_o \sqrt{1 + \left(\frac{z}{z_R}\right)^2}, \quad (5)$$

where $z_R = \frac{\pi {w_o}^2}{\lambda_L}$ is known as the Rayleigh length, which defines the point where the width of the gaussian beam has increased by a factor of $\sqrt{2}$ and the intensity has halved as shown in Figure 3. Figure 4 shows the evolution of the gaussian beam width as a function of the propagation

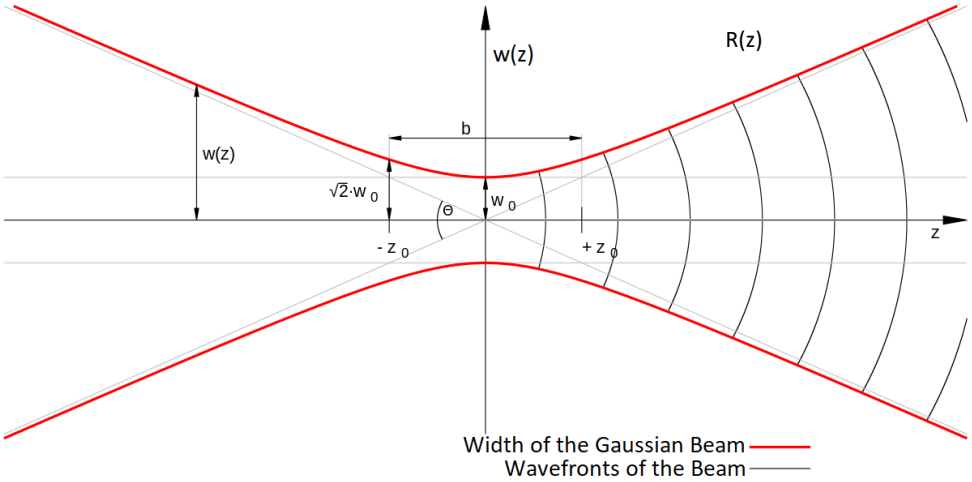

Figure 4: The evolution of the gaussian beam width along with the radius of curvature of the beam wavefront ($R(z)$) of the beam at different positions [14].

distance with the minimum width at the point of focus z=0. The longitudinal width of a gaussian beam can be defined as twice the Rayleigh length denoted as b in Figure 4. If the gaussian beam is focused strongly making w_o small, the Rayleigh length decreases implying that the beam starts to diverge more strongly. This is one of the inherent properties of the gaussian beam. Another property is the use of ABCD formalism from ray optics to calculate the beam width and the radius of phase curvature after passing through simple optical elements such as mirrors, lenses or

mediums of different refractive indices. The q-parameter (complex beam parameter) for a gaussian beam can be defined as [14]

$$\frac{1}{q(z)} = \frac{1}{R(z)} - \frac{i\lambda_o}{\pi n w(z)^2}, \tag{6}$$

where $q(z)$ is the q-parameter, $R(z)$ is the radius of curvature of the beam wavefront, λ_o is the beam's vacuum wavelength, n is the refractive index of medium and $w(z)$ is the width of the gaussian beam. The q-parameter of a gaussian beam passing through optical elements is related to the input beam q-parameter by just a matrix multiplication given by [14]

$$q_f = \frac{Aq_i + B}{Cq_i + D} \tag{7}$$

where A, B, C, D are the matrix elements of the ABCD matrix and q_i, q_f are the input and output q-parameters of the gaussian beam. The use of this matrix multiplication can be demonstrated by finding the size of the focal spot of a collimated gaussian beam incident on a thin lens as shown in Figure 5.

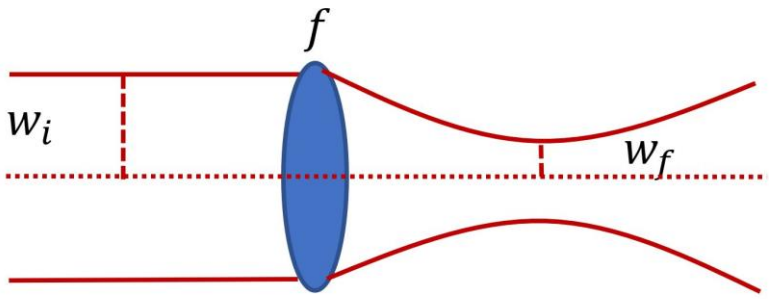

Figure 5: A collimated gaussian beam with an initial width of w_i being focused to a small spot with the final waist w_f.

The ABCD matrices to be used for such a calculation are those of a thin bi-convex lens with a focal length of f and of free-space propagation with a distance d [15].

$$Propagation\ Matrix = \begin{bmatrix} 1 & d \\ 0 & 1 \end{bmatrix} \tag{8}$$

$$Lens\ Matrix = \begin{bmatrix} 1 & 0 \\ \frac{-1}{f} & 1 \end{bmatrix} \tag{9}$$

The above matrices are first multiplied to get the final matrix for this optical system after which, equation 76 is used to get the final q-parameter. The final q-parameter relates to the width of the beam in the focal spot by equation 6, which is used to get the final waist of the gaussian beam as [14]

$$w_f = \frac{f\lambda}{\pi w_i} \tag{10}$$

where w_f and w_i are the final and initial width of the gaussian beam respectively. This result was used to adjust the area of illumination of the probing system, which will be discussed in a later section.

2.1.3 Spatial and Temporal Coherence

To interferometrically probe laser-generated plasmas with ultrashort pulsed beams it is necessary for the pulses to exhibit certain properties, which will be discussed in this section. Consider two light waves, which are superimposed each having the same frequency ω with different k-vectors and initial phases $\epsilon_1$and ϵ_2 given as [16]

$$\overrightarrow{E_T}(\vec{r},t) = \overrightarrow{E_{01}}\cos\left(\overrightarrow{k_1}.\vec{r} - \omega t + \epsilon_1\right) + \overrightarrow{E_{02}}\cos\left(\overrightarrow{k_2}.\vec{r} - \omega t + \epsilon_2\right). \tag{11}$$

The intensity of a light wave is proportional to the time-period average of the square of the electric field and is given as

$$I(\vec{r}) = I_1(\vec{r}) + I_2(\vec{r}) + I_{12}(\vec{r}) = \langle\overrightarrow{E_1^2}\rangle(\vec{r}) + \langle\overrightarrow{E_2^2}\rangle(\vec{r}) + 2\langle\overrightarrow{E_1}.\overrightarrow{E_2}\rangle(\vec{r}) \tag{12}$$

The third term in equation 12 is known as the interference term which can be evaluated in this instance by taking the dot product of the two individual fields and then time averaging the cosines to get [16]

$$I_{12}(\vec{r}) = \overrightarrow{E_{01}}.\overrightarrow{E_{02}}\cos\delta, \tag{13}$$

where $\delta = \overrightarrow{k_1}.\vec{r} + \epsilon_1 - \overrightarrow{k_2}.\vec{r} - \epsilon_2$ is the phase difference arising from the different path lengths and initial phase-angle difference. From equation 13 for two orthogonal polarizations the interference term vanishes, implying similar (or non-orthogonal) polarizations for interference to be seen. From equation 12 it can be noted that similar intensities in both the waves is also required for the interference term to be visible. If one of the beams is of a much higher intensity, then the interference term is hidden under the stronger signal. Two other important conditions

that need to be satisfied to see the interference term is the high degree of spatial and temporal coherence. The temporal coherence is the ability of the electromagnetic radiation to maintain a fixed phase relationship and be predictable when measured at a fixed spatial point but different points in time. The temporal coherence is a manifestation of the spectral purity of a laser pulse, the purer or more single colored light pulse there is the more temporally coherent it will be. It is mathematically proportional to the inverse of the bandwidth of the laser pulse [17]

$$\tau \propto \frac{1}{\Delta\nu} \propto \Delta t \tag{14}$$

where τ is the coherence time, Δt is the pulse duration and $\Delta\nu$ is the frequency bandwidth of the pulse. Equation 14 implies a decrease in the coherence time of the pulse as the pulse duration is decreased. Another quantity used to describe the degree of temporal coherence is the coherence length that is the distance travelled by the light in the coherence time. If the spectral phase of a pulse is frequency-independent, it is said to be Fourier-transform limited (FTL). For FTL pulses having a Gaussian spectrum the coherence length is given as [18]

$$L_c = \sqrt{\frac{2\ln(2)}{\pi n}}\frac{\lambda^2}{\Delta\lambda}, \tag{15}$$

where λ is the central wavelength of laser source, n is the refractive of the medium and $\Delta\lambda$ is the FWHM of the laser source. For quasi-monochromatic laser sources, the coherence length is on the order of meters while for ultrashort pulses the coherence length is on the order of microns. This is important while aligning an interferometer, since for interference to be seen at the detector, the path difference between two pulsed beams needs to be less than the coherence length.

The spatial coherence is defined as the ability of the electromagnetic radiation to maintain a fixed phase relationship and be predictable when measured across space at a fixed point in time. The two beams being interfered need to have high spatial coherence to get an observable interference pattern because at points where the amplitude is not predictable (hence low spatial coherence) the interference pattern will diminish [16].

2.2 Plasma Generation and Plasma Parameters

This work focuses on probing the dynamics of laser-generated plasmas, for which it is important to understand the underlying physics of plasma generation from electromagnetic fields.

2.2.1 Ionization Mechanisms

A material is ionized when its bound electrons attain enough energy to escape the Coulomb potential. This is described in the simplest case by the classic photoelectric effect, which predicts the generation of a photoelectron and thus ionization of the material, if the energy of the photon (depending upon the frequency f) becomes greater than the work function (φ) of the metal ($E_{photon} = hf > \varphi$) [19]. Aluminum (Al), the principal material being used in this work to create plasma, has a work function of about 4.28eV while the energy of a photon with wavelength 1.03µm being used in this work is 1.20eV [20]. Thus, Al cannot undergo ionization by the classic photoelectric effect.

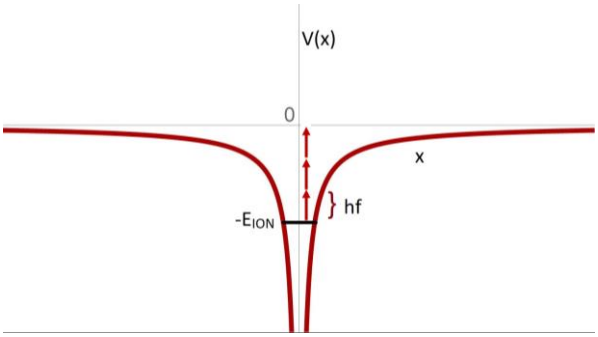

Figure 6: Multiphoton Ionization where 3 photons are absorbed at the same time by the electron to escape coulomb potential.

Nevertheless, there are 3 other mechanisms by which the Al used in this work undergoes ionization namely multiphoton ionization (MPI), tunneling ionization and over the barrier or barrier suppression ionization (BSI). When the intensity of the light is high enough ($I > 10^{10}\mathrm{Wcm}^{-2}$), there is a high probability of more than one photon being absorbed at the same time by the electron. This phenomenon shown in Figure 6 depicts the process with 3 photons being absorbed to release a bound electron from the coulomb potential. MPI is considered a perturbative process where it is assumed that the laser field does not have any effect on the atomic potential [21]. This assumption breaks down when the laser field is increased further ($I \sim 10^{14}\mathrm{Wcm}^{-2}$) and the laser field starts to tilt the coulomb potential in both directions over one cycle. During half the cycle of the laser field the barrier shown in Figure 6 is lowered

forming a potential barrier between the bound electron and the continuum outside through which an electron can tunnel. This mechanism is known as Tunneling Ionization. The interplay of MPI and Tunneling ionization is captured in the Keldysh parameter γ [22]

$$\gamma = \omega_L \sqrt{\frac{2E_{ion}}{I_L}} \tag{16}$$

where ω_L is the laser frequency, E_{ion} is the Ionization energy and I_L is the laser intensity. For a Keldysh parameter $\gamma > 1$ MPI applies, while for $\gamma < 1$ Tunneling ionization applies, although this difference becomes cloudier for multi electron systems due to screening [23]. A simple formulation of the modified coulomb potential is given as [21]

$$V(x) = -\frac{Ze^2}{x} - e\varepsilon x \tag{17}$$

where $V(x)$ is the modified atomic potential, Z is the atomic number, e is the charge of an electron and ε is the amplitude of the laser electric field. This modified potential can be differentiated to find the position x_{max} of the potential barrier shown in Figure 7 [24]. Equating the $V(x_{max}) = E_{ion}$ gives the critical laser field amplitude after which the barrier falls below E_{ion} and the electron can escape spontaneously from the atom.

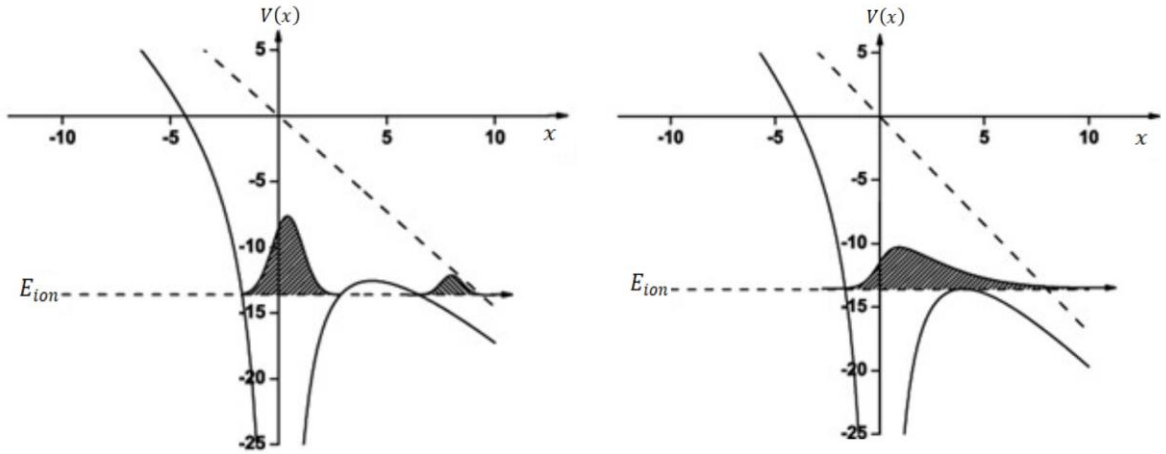

Figure 7: The image on the left shows the potential being modified and acting as a potential barrier for the electron, which now has a non-zero probability on the other side and can tunnel through. On the right is the barrier being suppressed at even higher intensities and the electron can freely pass through and leave the atomic potential [24].

This is known as Barrier suppression Ionization (BSI) and the corresponding critical electric field ε_c at which it occurs is given as [21]

$$\varepsilon_c = \frac{{E_{ion}}^2}{4Ze^3}. \quad (18)$$

The optical intensity at which this critical field is achieved known as appearance intensity (I_{app}) can be calculated as follows [21]

$$I_{app} = \frac{c}{8\pi}{\varepsilon_c}^2 \sim 4 \times 10^9 \left(\frac{E_{ion}}{eV}\right)^4 Z^{-2} W cm^{-2}. \quad (19)$$

Equation 19 can also be applied for the case of Aluminum, which serves as the principal target in this setup. The appearance intensity required to triply ionize the Aluminum calculated from equation 19 is about 3×10^{14} $\mathrm{Wcm^{-2}}$, about 2 orders of magnitude lower than the intensity being used in this work. This model does not consider the neighboring atoms, which can also have an influence on the atomic potential and thus this value is an ideal estimate only. Another form of ionization known as collisional electron ionization [25] dominates in solid metals such as Aluminum after the initial ionization process due to a large amount of quiver energy given to the electrons by the ponderomotive force of the laser field. This energy U_p is given as [26]

$$U_p = 9.33 \times 10^{-14}(I_L \lambda^2)\mathrm{eV}, \quad (20)$$

where I_L is the laser intensity and λ is the laser wavelength. At laser intensities of $10^{16} W cm^{-2}$ and a wavelength of $1.03 \mu m$ being used in this work, this energy is $990 eV$. This amount of energy is enough to ionize the Aluminum atoms with electron collision ionization from Al^{1+} with an ionization potential of $6eV$ to Al^{11+}, which has an ionization potential of $442eV$ [26]. This implies the dependence of the plasma parameters on the wavelength and the intensity of the laser field.

2.2.2 EM Wave in Plasma

So far, the different mechanisms for the creation of a plasma from a solid Aluminum target were discussed. This section takes a look at related plasma parameters, and their meaning, within the context of electro-magnetic wave propagation through plasma. Plasma is mainly composed of a large number of electrons and ions, exhibiting different collective behavior, one of which are plasma oscillations. These oscillations are of electron densities against a uniform ion background defining a characteristic plasma frequency ω_p, which has consequences shown later in this section, for a laser pulse trying to penetrate a plasma. These plasma oscillations can be described by the well-known Drude model for metal optics, since the electrons here are considered as free charges without a restoring force [27].

$$\frac{\partial^2}{\partial t^2} s(\vec{r},t) + g\frac{\partial}{\partial t} s(\vec{r},t) = -\frac{e}{m_e}\vec{E}(\vec{r},t). \quad (21)$$

Here $s(\vec{r},t)$ is the electron displacement, g is the damping constant, e is the charge of the electron and m_e is the mass of an electron. In the equation above the driving force does not have the contribution from the magnetic field, since in the non-relativistic case it is approximately $\frac{v_e}{c}$ times less than the $\vec{E}$ field. Another assumption made here is a static ionic background and the thermal energy of the electrons is also ignored so the oscillations do not travel through the plasma. The current density $\vec{j}(\vec{r},t)$ induced by the movement of the electrons is given by [28]

$$\vec{j}(\vec{r},t) = -n_e e\frac{\partial}{\partial t} s(\vec{r},t), \quad (22)$$

where n_e is the electron density. With this equation 21 becomes

$$\frac{\partial}{\partial t}\vec{j}(\vec{r},t) + g\vec{j}(\vec{r},t) = \frac{e^2 n_e}{m_e}\vec{E}(\vec{r},t) = \varepsilon_0 {\omega_p}^2 \vec{E}(\vec{r},t), \quad (23)$$

where ω_p is the plasma frequency given as

$$\omega_p = \sqrt{\frac{e^2 n_e}{\varepsilon_0 m_e}}. \quad (24)$$

Taking the Fourier transform of equation 23, solving for $\vec{j}(\vec{r},\omega)$ and comparing it with $\vec{j}(\vec{r},\omega) = \sigma(\omega)\,\vec{E}(\vec{r},\omega)$ results in the following complex frequency dependent conductivity

$$\sigma(\omega) = \frac{\varepsilon_0 {\omega_p}^2}{g - i\omega} = -i\frac{\varepsilon_0 \omega {\omega_p}^2}{-\omega^2 - ig\omega}. \quad (25)$$

From the theory of electromagnetic wave, in the absence of bound electrons the generalized complex dielectric function is given as [27]

$$\varepsilon(\omega) = 1 + \frac{i}{\omega\varepsilon_0}\,\sigma(\omega) = 1 + \frac{{\omega_p}^2}{-\omega^2 - ig\omega}. \quad (26)$$

The refractive index is related to the real part of the complex dielectric function and is given by [29]

$$\eta(\omega) = \sqrt{\acute{\varepsilon}(\omega)} = \sqrt{1 - \frac{{\omega_p}^2}{{\omega_L}^2}} \quad (27)$$

where ω_L is the frequency of the laser field and ω_p is the plasma frequency. The above depicts the refractive index as seen by an electromagnetic wave propagating through a plasma. The refractive index is real for laser frequencies greater than the plasma frequency implying that the laser field decays evanescently if the laser field is lower than the plasma frequency. This in turn allows a critical density of electron to be defined at which the laser field of a particular frequency ω_L is reflected. Using equation 24 the critical density n_c can be defined as [30]

$$n_c = \frac{\varepsilon_0 m_e \omega_L}{e^2} = 1.1 \times 10^{21} \left(\frac{\lambda_L}{\mu m}\right) cm^{-3}. \tag{28}$$

For the central wavelength of the laser field being used in this work ($\lambda_L = 1.03\mu m$) the critical density is $n_c = 1.133 \times 10^{21} cm^{-3}$. Using this the refractive index can be written as a ratio of the electron density to the critical density instead of as a ratio of frequencies.

$$\eta(n_e(x,y,z)) = \sqrt{1 - \frac{n_e(x,y,z)}{n_c}} \tag{29}$$

The plasmas which have an electron density less than the critical are known as underdense plasmas while those with an electron density more than the critical are known as overdense plasmas. In overdense plasmas, the refractive index becomes imaginary and thus the electric field evanescently decays and in 1D under normal incidence given as

$$E(x) = E(0) \exp\left(-\frac{x}{l_s}\right), \tag{30}$$

where $l_s = \frac{c}{\omega_p}\left(1 - \frac{\omega^2}{{\omega_p}^2}\right)^{-\frac{1}{2}}$ is termed as the skin-depth. This is the characteristic penetration depth of the electromagnetic field inside an overdense plasma, which for highly overdense plasmas is approximated by $l_s \approx \frac{c}{\omega_p}$.

2.3 TNSA Process

The importance of studying the plasma properties can be put into perspective with the knowledge of ion acceleration mechanisms. The current high-powered Petawatt laser systems reviewed by Danson et.al [31] can generate intensities on the order of 10^{21}W/cm^2. An electron

in a laser field can be directly accelerated to relativistic velocities if a threshold intensity given as [32]

$$I_L {\lambda_L}^2 = 1.37 \times 10^{18} \frac{\mathrm{W\mu m^2}}{cm^2} \tag{31}$$

is crossed. This allows the electrons to be accelerated directly by the laser systems currently around the world. A similar threshold for the protons can be derived, which is higher due to higher mass of the protons requiring a larger force [32].

$$I_L {\lambda_L}^2 = 5 \times 10^{24} \frac{\mathrm{W\mu m^2}}{cm^2} \tag{32}$$

This higher threshold of protons and even higher for heavier ions eliminates the possibility of directly accelerating these ions in a laser field for current Petawatt laser systems. A possible

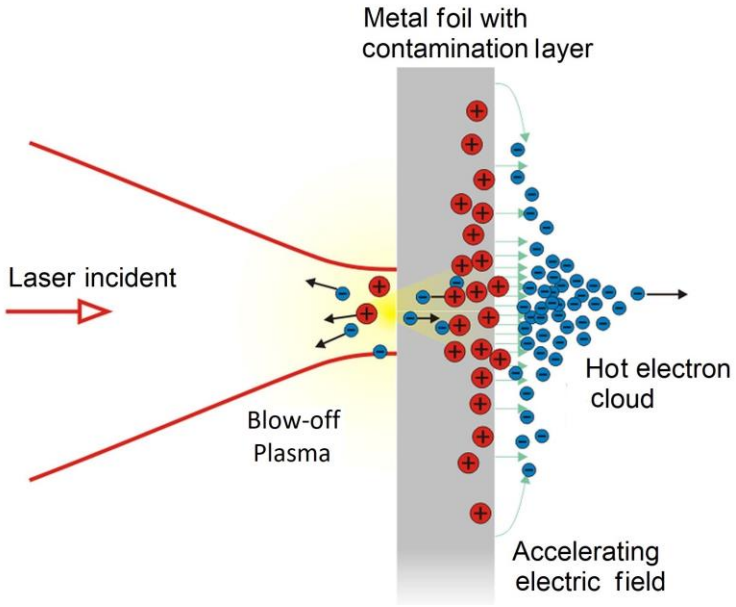

Figure 8: The basic schematic of TNSA process. The laser is incident from the left, the blow-off plasma is created by a pre-pulse or amplified spontaneous emission (ASE) which arrives at the target before the main laser pulse.

mechanism to accelerate ions by using hot electrons to mediate the transfer of energy from the laser field to ions is termed as Target Normal Sheath Acceleration (TNSA) [33]. By hot electrons in the context of TNSA, one means the relativistic electrons, which have the energy on the order of the laser ponderomotive potential travelling in the laser forward direction. The basic schematic of this process using thin metallic foils is shown in Figure 8 and can be explained in a series of steps as follows [34]

[1] Since the main laser pulse being focused on the metallic target is on the order of 10^{21}W/cm^2, a pre-pulse or amplified spontaneous emission (ASE) from amplifier stages of the order of 10^{14}W/cm^2 is enough to ionize the target and create a pre-plasma. This pre-plasma blows off the surface of the target and expands in the direction of the incoming laser.

[2] The main laser pulse arrives and interacts with the pre-plasma and transfers energy to the plasma electrons. The absorption of the main laser pulse greatly depends on the properties of the pre-plasma.

[3] Hot electrons are generated after absorbing the laser energy in the forward direction and propagate through the target and escape from the rear surface of the target. This process continues untill a positive sheath on the rear side stops more electrons from escaping creating a space-charge field.

[4] The ions are then accelerated, normal to the rear surface of the target, under these space-charge fields to energies of mega electron volts (MeV) [34]. A contamination layer which is rich in protons is usually applied on the rear surface to facilitate ion acceleration.

The main component in the above process is the generation of hot electrons which determine the strength of the space charge fields. The conversion of laser energy into hot electrons is governed by a number of different absorption mechanisms depending upon the laser and target parameters. Two of the main parameters that significantly change the absorption physics are the scale lengths L and the intensity I_L.

2.3.1 Collisional Absorption

When a laser field with an intensity >10^{14}W/cm^2 is incident on a metallic target, in this work Aluminum, it is ionized, and the laser energy is then either absorbed or reflected off this solid density plasma. At such a moderate intensity (by modern standards) collisional absorption is the dominant mechanism in coupling laser energy to the target [30]. Possible binary collisions in a 2-particle plasma consisting of ions and electrons are: electron-electron collisions which serve to increase the plasma temperature, ion-ion collisions are negligible due to ions not responding to laser field in the short timescales considered here (≈ ps) and electron-ion collisions that allows the electrons to deposit energy in the target lattice. The main quantity governing the strength of collisional absorption is the electron-ion collisional frequency v_{ei} given as [35]

$$v_{ei} = 2.91 \times 10^{-6} Z n_e T_e^{-\frac{3}{2}} \ln \Lambda \ \mathrm{s}^{-1} \tag{33}$$

where Z is the number of free electrons per atom, n_e is the electron density in cm^{-3}, T_e is the plasma electron temperature in eV and $\ln \Lambda$ is the Coulomb logarithm that accounts for the maximum and minimum limits of electron-ion scattering cross-section. In the regime of femtosecond laser pulses (used in this work), the laser pulse directly accesses solid density plasmas due to almost negligible hydrodynamic expansion. In this scenario, the laser pulse peak experiences an almost a step like density profile $\left(\frac{L}{\lambda} \leq 0.1\right)$, where the plasma is highly collisional due to a higher density. The Helmholtz equations can be solved to derive the absorption fraction due to the electron ion collisions and is termed as the normal skin effect (NSE) when the collisions take place within the skin depth of the electric field.

2.3.2 Resonance Absorption

Collisional absorption starts to decrease as implied by equation 33 when the temperature of the plasma starts to increase. Resonance absorption is a collisionless absorption mechanism with which the laser energy can be coupled to the plasma with long scale lengths $(L \gg \lambda)$. The resonance absorption is most efficient when the plasma frequency is equal to the laser frequency [36]. A p-polarized laser pulse incident on the target with an angle of θ is constantly deflected by the plasma electron gradients as shown in Figure 9. As a result, the Electric field of this laser pulse is also constantly tilted and at the turning point of the laser beam, where the density

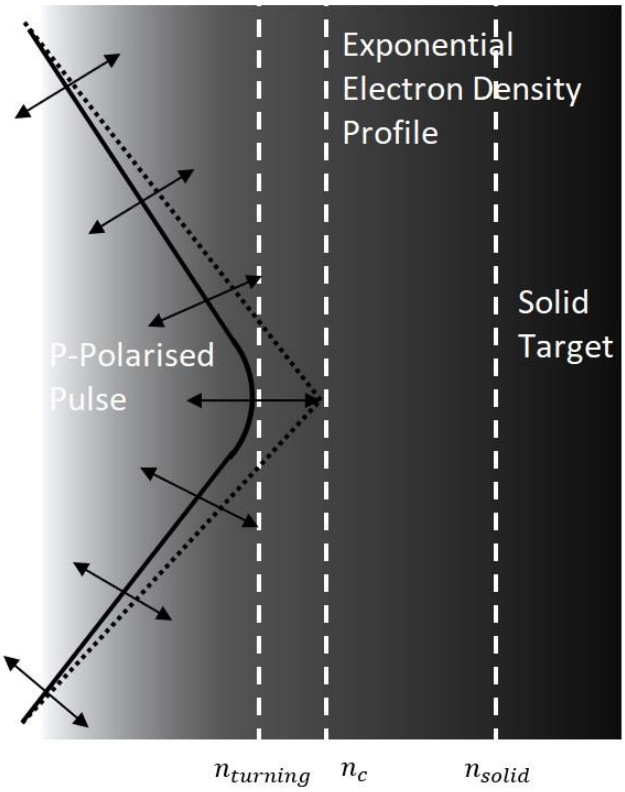

Figure 9: Resonance Absorption at the turning point where the evanescent E-field oriented along the gradient of plasma electron density tunnels through and excites plasma waves.

is $n_{turning} = n_c \cos^2 \theta$, the electric field aligns with the electron density gradient, tunnels through and excites plasma wave. Since, these plasma waves grow over the laser cycles, the amplitude of the wave increases until the wave breaks, dampens and generates hot electrons that propagate through the target.

2.3.3 Vacuum Heating

Vacuum heating is another collision less absorption mechanism that plays a dominant role in steep gradient plasmas $(L < 0.1\lambda)$. When a p-polarized laser pulse is incident with an angle θ on the target, the electric field has a component in the direction of the plasma electron density gradient. The electrons at the abrupt vacuum-plasma interface then directly interact with the laser electric field. In the first half of the electric field cycle, it accelerates the electrons out into the vacuum and then accelerates them back inside the target when the field reverses sign. Since the target is overdense, the electric field evanescently decays inside the solid target and cannot follow the electron which is absorbed inside the target through collisions [37]. The absorption

fraction of the laser field due to vacuum heating changes as the incidence angle of the laser pulse is varied and is under 1% for incidence angles of <10° [30].

2.3.4 Anomalous Skin Effect (ASE)

Anomalous Skin Effect (ASE) is the third collision less mechanism of laser absorption discussed in this work. This effect contributes to the laser absorption by effectively increasing the skin depth, where the electrons are absorbed through collisions with ions. In the case of steep gradient plasmas, the electrons within the skin depth of the electric field oscillate and dissipate energy through electron-ion collisions. This is termed as the normal skin effect (NSE) in which, the electron mean free path [30] $\lambda_{mfp} = \frac{v_{te}}{\nu_{ei}}$ and the mean excursion length of the electron $d_{mel} = \frac{v_{te}}{\omega_L}$ both, are smaller than the skin depth $l_s = \frac{c}{\omega_p}$ given by equation 30. The effect of the electric field is thus not felt at distances larger than the skin depth. Consider a case now where the temperature of the electrons is increased which, consequently, increases the mean free path as well as the mean excursion length of the electrons such that it becomes greater than the skin depth. These electrons carry the effect of this electric field at larger distances effectively increasing the skin depth of the electric field. This results in an increase in absorption due to larger skin depths increasing the probability of electron-ion collisions. The new skin depth l_a is derived considering this nonlocal relationship of electric field and induced current and is given by [38]

$$l_a = \left(\frac{2}{\pi}\right)^{1/6} \left(\frac{c^2 v_{te}}{\omega_L \omega_p^2}\right)^{1/3} \tag{34}$$

where v_{te} is the thermal velocity of the electron, ω_L and ω_p are the laser and plasma frequencies. This effect is more prominent under normal incidences where the Vacuum heating and resonance absorption plays a less significant role.

2.3.5 JxB Heating

The last collisionless mechanism for laser absorption into the plasma considered in this work is the jxB heating [39]. This mechanism is similar to vacuum heating and requires steep plasma gradients. While vacuum heating relies on the E-field of the electromagnetic wave to extract electrons, the jXB heating relies on the vxB term of the Lorentz force to extract electrons. For low intensities when the motion of the electron can be considered classic this mechanism is negligible owing to small amplitude of the vxB term. For intensities in excess of 10^{18} W/cm^2, this mechanism

becomes dominant and under normal incidence can be very efficient in coupling laser energy into the target. The main difference of this mechanism from the vacuum heating is a higher oscillation frequency of the vxB term 2ω, while the Electric field varies with a frequency of ω. This mechanism works for both S and P polarized light, even under normal incidence, while for circularly polarized light under normal incidence this effect is suppressed. This happens due to opposing vxB forces generated by the s and p polarized components of a circularly polarized light.

3 Experimental Setup

In this section, the experimental setup utilized in this work to interferometrically probe laser generated plasmas is discussed. One of the advantages of the experimental setup is its ability to probe the laser-generated plasmas at two different times in a single shot. This is achieved by splitting the spectrum of the probe pulse and delaying one part to generate two pulses from a single pulse. These two pulses are then sent to the interaction region, after which they are separated with a similar setup and sent to the interferometer to obtain phase information. This results in access to two controllable time steps of the plasma expansion.

The section is divided into three main parts shown in Figure 10: the first part discusses the probe pulse and the two temporal and spatial separation devices along with the interferometer used in this work, the second part discusses the pump pulse, the third part discusses the geometry of the target that was utilized in this work to generate plasmas. A laser pulse coming from a regenerative amplifier is passed through a 90:10 Beamsplitter resulting in a pump pulse (90% energy) and a probe pulse (10% energy).

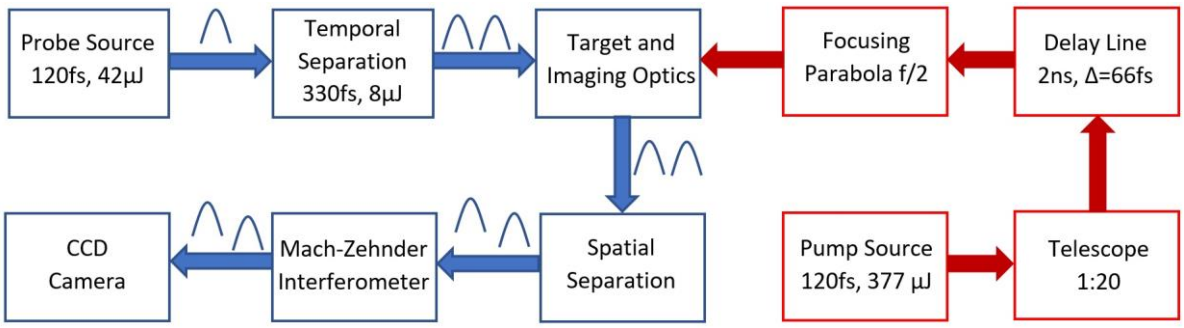

Figure 10: The general schematic of the experimental setup with the components of the probe pulse shown in blue and those of pump pulse shown in red.

3.1 Probe Pulse

The probe pulse source generates a pulse with a central wavelength of 1030 nm with a bandwidth of 15nm. The repetition rate for the amplifier is 1 Hz and the temporal duration (Full width half maximum) of the pulse is around 120 fs measured by an autocorrelator. The energy in the probe pulse is varied during the energy scan and is about 40μJ when the energy of the regenerative amplifier output is kept to a maximum. This probe pulse is then directed into an optical setup, named temporal separation device, which generates two pulses with a variable delay in between.

3.1.1 Temporal Separation Device

The temporal separation device, depicted in Figure 11 consists of a grating, an imaging lens and two small mirrors one of which, can move to allow temporal separation of a part of the pulse.

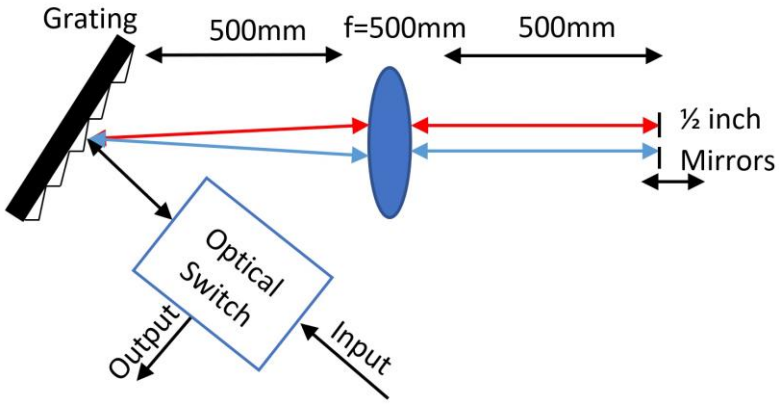

Figure 11: The top view of temporal separation device schematic where one of the half inch mirrors is movable to allow for a delay and temporal separation of a part of the pulse.

The input path is separated from the output path by an optical switch that consists of a faraday rotator and a polarizer. The principle of the setup is as follows: the input pulse hits the grating and goes through a 4f imaging setup built from grating back to grating with small half inch mirrors placed in the Fourier plane. In the Fourier plane, the beam is spatially focused but spectrally dispersed. Here the gaussian spectrum of the initial pulse is modified by these two mirrors, the peak of the spectrum passes through the gap and is not reflected while the other parts of the gaussian spectrum are reflected from each mirror as shown in Figure 12. By displacing one of the mirrors, the path of half of the gaussian spectrum is changed that results in a temporal separation. The duration of the pulses is increased, which was expected since their spectrum has been reduced. The pulse duration after the temporal seperation device of each pulse is about 330±10 fs. This pulse duration is sufficient to probe the hydrodynamic expansion of the plasma

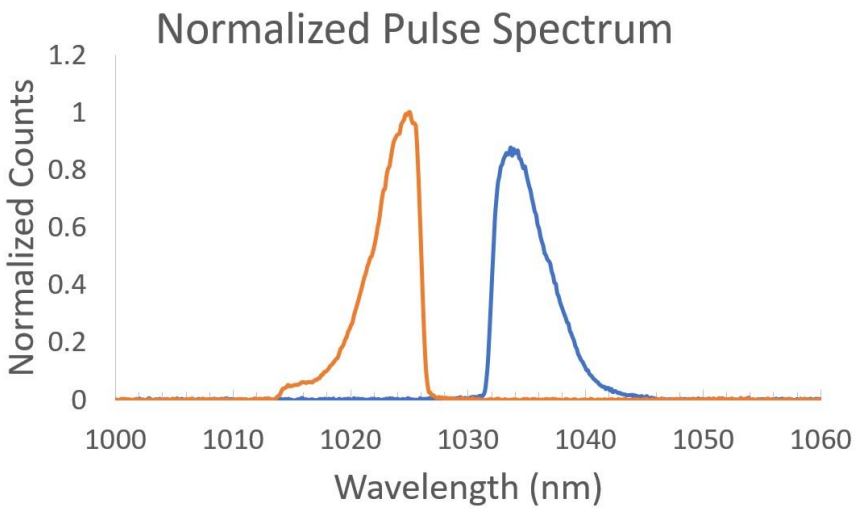

Figure 12: The Spectrum of the two pulses after the temporal separation setup. Each of the pulse has one part of the gaussian spectrum and is abruptly cut off due to the mirror edge. The center part of the spectrum is lost and is not seen in either of the pulses.

that is negligible on the fs timescales. One important requirement of this temporal setup is to have the pulses travel back in the same direction and position as shown in Figure 13. If this is violated, the pulses would get an additional delay and would also illuminate different spatial points in the interaction region. The delay between the pulses can be achieved in steps of 67 fs for a total delay of 166ps. Figure 13 also depicts the decrease in the spatial size of the beam after the lens.

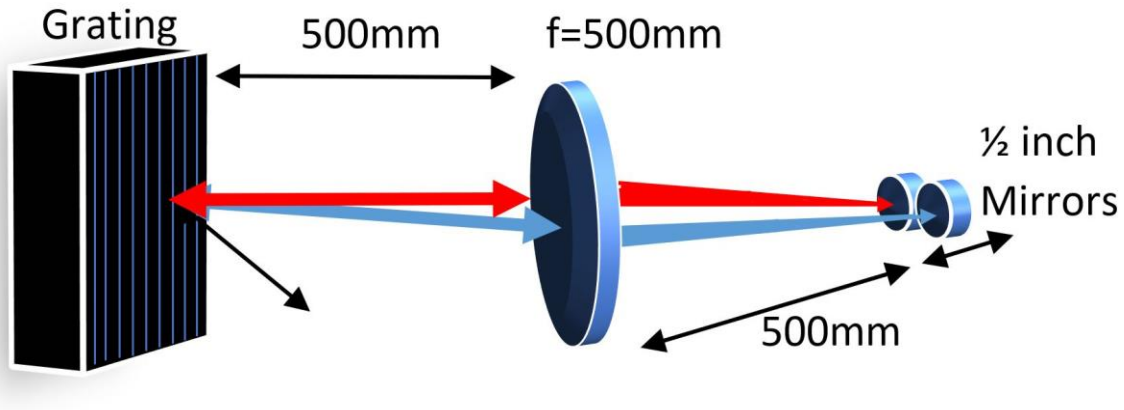

Figure 13: The side view of the temporal separation device depicting the same path travelled by the pulses when being reflected from the small mirrors after the lens. The spatial size of the beam decreases after the lens that is depicted here by the decreasing size of the red and blue beam.

3.1.2 Imaging System

The pulses after the temporal separation device are focused by imaging optics into the interaction region where the target is kept as shown in Figure 14. The first lens in the schematic controls imaging parameters such as depth of field and the field of view. When the focal length of the lens is increased the field of view and the depth of field increases at the expense of image quality. The image quality becomes poorer because of different divergence of the image information and the beam.

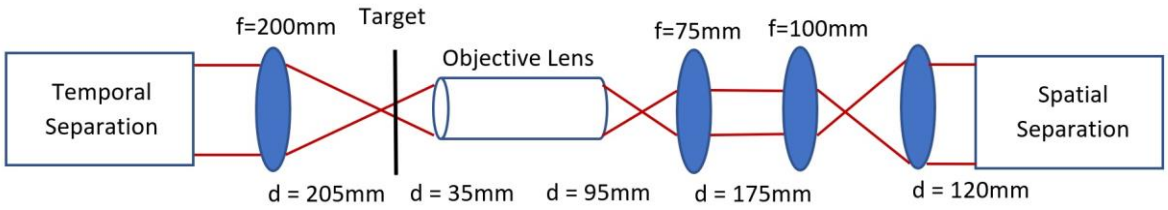

Figure 14: The probe pulse from the temporal separation device is then focused towards target to illuminate interaction region and then collected by objective. Subsequent relay lenses are used to maintain image quality over a large distance.

A measure of image quality used in this work as a criterion is the resolution determined by 1951 USAF resolution test target shown in Figure 15 [40]. Resolution of the imaging system is higher if

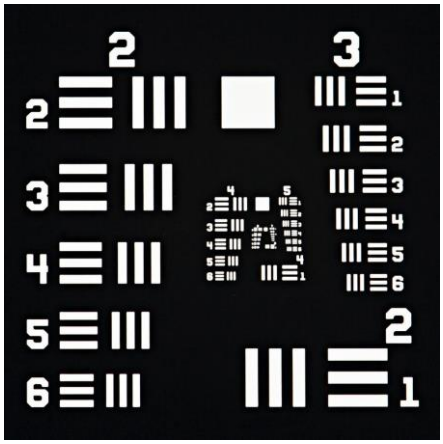

Figure 15: A standard resolution test target used to determine the experimental spatial resolution of the probe pulses.

smaller lines on this target can be distinguished. A theoretical measure of the highest resolution achievable by the imaging system can be calculated using Abbe's resolution limit [41] given as

$$d = \frac{\lambda}{2NA} \tag{35}$$

where λ is the wavelength of light being used, NA is the numerical aperture of the objective being used to collect light from the object and d is the minimum feature size that can be observed in the image plane. For the current work, a Mitutoyo M PLAN Apo NIR 10x objective was used that results in a diffraction limited resolution of 2µm while the experimental resolution measured using USAF chart is of 3.5µm. The reason for a larger value is loss of image information in the spatial separation device (see chapter 3.1.3), where half-inch mirrors cut off image information. Despite this the plasma is observed after 20 ps when the scale lengths are larger, thus, the spatial resolution is sufficient to observe plasma dynamics. The field of view of the imaging system is kept to 150µm, resulting in a depth of field of 7µm. The field of view is kept larger deliberately so as to have a part of the beam which is undisturbed by plasma phase information. The magnification of the system can be adjusted by the focal lengths of the lenses used after the objective to relay the image information. The magnification factor is kept to a value of 27 to observe the plasma scale lengths on the order of few µm.

3.1.3 Spatial Separation Device

After the pulse has passed the target region, it passes to the spatial separation device shown in Figure 16. The spatial separation device is similar to the temporal separation with minute differences. Firstly, the two small mirrors are now fixed as opposed to a movable mirror in the temporal separation device. Secondly, there is no optical switch since the input and the output beams have no requirement to be sent back at the same path as the temporal separation device. Lastly, the input pulses and output pulses are spatially separated by a tilt introduced in the small

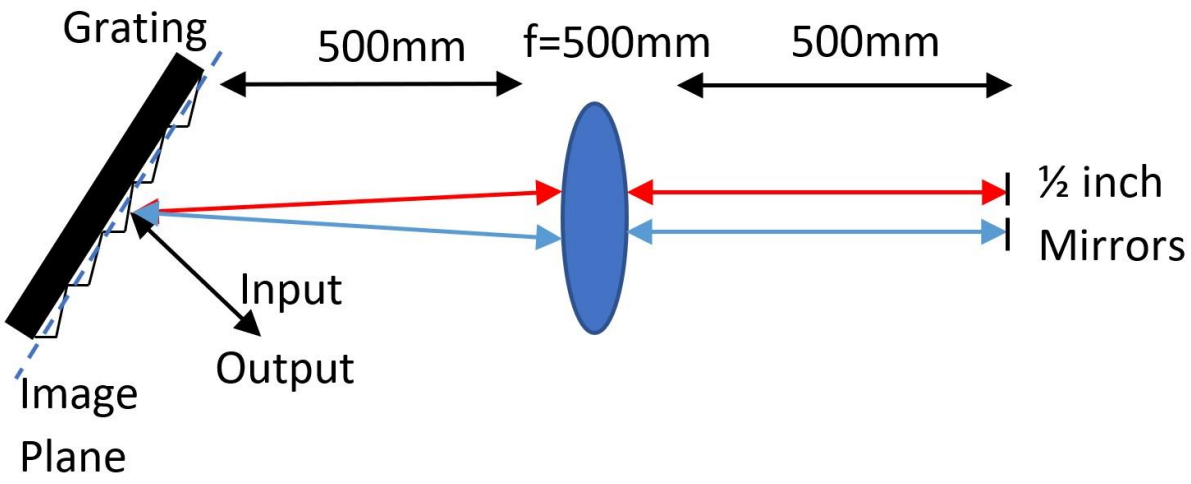

Figure 16: The top view of spatial separation device where both the small mirrors are now fixed but tilted to send the two pulses back at different spatial points.

mirrors, which can be better seen in the side view shown in Figure 17. After the beams have been spatially separated, they are sent to the interferometer and then subsequently imaged onto the CCD to obtain two-time step information in a single shot on two different CCD chips.

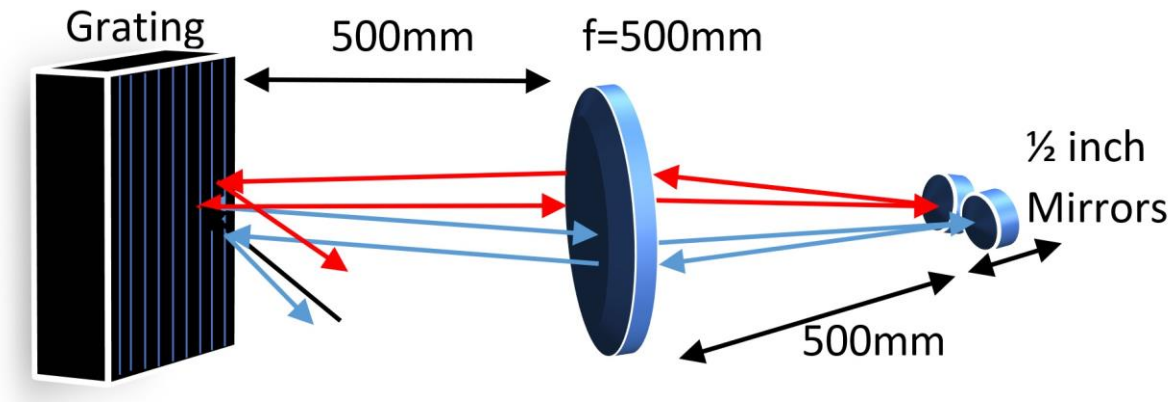

Figure 17: The side view of the spatial separation device where it can be clearly seen that the input and the output pulses are spatially separated.

3.1.4 Mach-Zehnder Interferometer

A Mach-Zehnder Interferometer shown in Figure 18 with one delay stage was assembled and utilized to obtain the phase information from the interaction region. The pulses are relayed

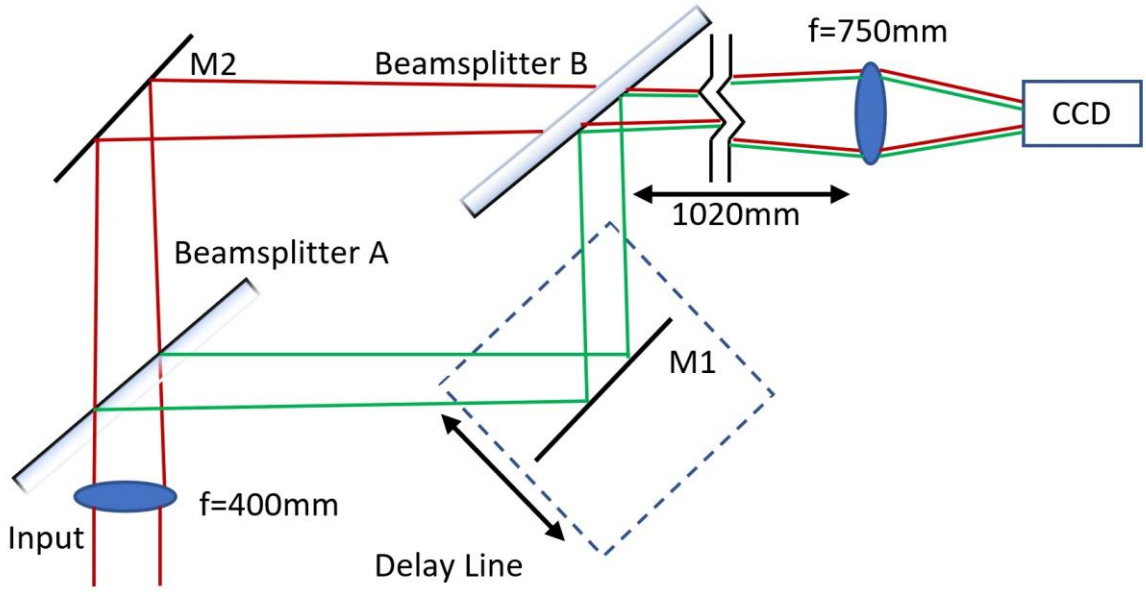

Figure 18: A Mach-Zehnder Interferometer showing the path of one of the pulses and the last relay lens used to image the interaction region onto the CCD. For the second pulse a second but similar CCD is used.

through the interferometer but induce little change in beam divergence due to the length of the

interferometer (≈ 13cm) being much smaller than the focal length of the lens (= 40cm) before the interferometer. The interferometer in this case was used to create a shearing geometry shown in Figure 19 where the overlap of the disturbed and the undisturbed part gives access to plasma

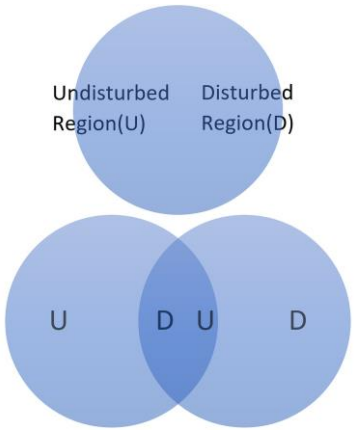

Figure 19: The shearing profile created to gain access to the phase information from the interaction region.

phase information. The main requirement for this method to work is sufficient undisturbed section of the beam, which is achievable by increasing the field of view. The field of view of 150µm was seen to be sufficient to make use of the shearing geometry and get accurate phase information from the interaction region. The interferometer was first alligned using a CW laser with a central wavelength of 1030nm to get a null fringe. Then the interferometer alignment was optimized using M2 and Beamsplitter B to result in a higher number of fringes. After this alignment was completed, the ultrashort pulses were sent through the interferometer and the fringes dissapear due to a larger path difference between two arms of the interferometer than the coherence length of the pulse. The delay line was then adjusted to get visible fringes again and best contrast for both of the pulses. After the interferometer, each of the two pulses were imaged onto two different CCDs.

3.2 Pump Pulse

The pump pulse comes from the same regenerative amplifier as the probe pulse with a central wavelength of 1030 nm with a FWHM bandwidth of 14nm. The repetition rate for the amplifier is 1Hz and the pulse duration (Full width half maximum) of the pump pulse is kept fixed throughout this work to a value of 120fs. The energy of this pulse is varied from 54µJ to 377µJ from the amplifier to achieve different intensities. The optical setup of the pump pulse is shown in Figure 20 where it first passes through a delay line, which is used to adjust the pump and probe

pulse delay. The delay can be adjusted in step sizes of 67fs for a total delay of 2ns. Afterwards, the pump pulse is expanded using a 1:20 telescope to achieve a smaller focus by the focusing parabola. This effect can be seen from equation 10 where the initial waist of the beam is inversely

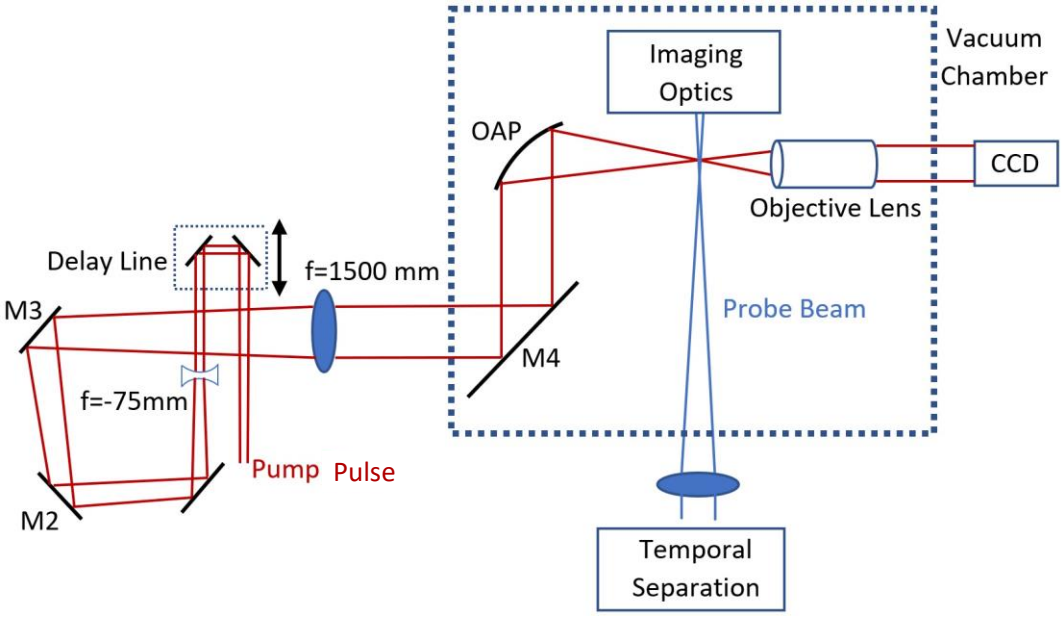

Figure 20: The optical setup showing the complete pump pulse setup and part of the probe pulse. The main components in the pump pulse are the delay line and telescope.

related to the waist of the beam after the lens. The beam is then focused inside a vacuum chamber by an f/2 off-axis parabola. This beam is imaged using a Mitutoyo M PLAN Apo NIR 20x objective shown in Figure 21 to align the parabola and to obtain the beam area. The focus area calculated by using the FWHM width is about $10\mu m^2$, waist (FWHM) is 1.8µm and the Rayleigh length consequently is 9.5µm. The waist measured experimentally is greater than that predicted by equation 10 (=0.7µm), because of wavefront and chromatic aberrations originating from the lenses in the setup, and the regenerative amplifier used to generate pump and probe pulses.

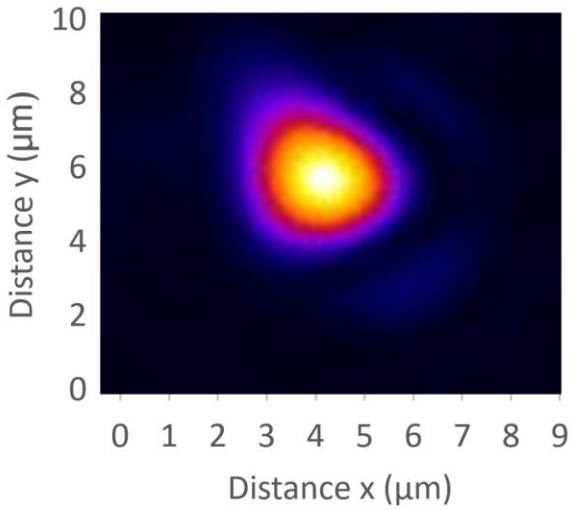

Figure 21: The image of the pump pulse focal spot imaged by a 20X objective.

The energy of the beam is measured by a pyroelectric energy sensor. With the measured energy, pulse duration and the area, the average intensity inside the FWHM beam width can be estimated using the relation [14]

$$I = \frac{E \,.\, q_{FWHM}}{A_{FWHM} \,.\, \tau_{FWHM}} \tag{36}$$

where E is the energy in the pulse, q_{FWHM} indicates the proportion of energy contained in the FWHM area that is 0.39 in this case and about 0.5 for an ideal Gaussian beam focus, A_{FWHM} is the area of the pulse that is obtained using the FWHM width and τ_{FWHM} is the FWHM pulse duration. The intensity here is an average intensity that is considered to be the same over the FWHM beam width. The area and the pulse duration for this work is kept fixed and only the energy of the pulse is varied to change the intensity. From Figure 20, it can also be seen that the Off-axis parabola (OAP) is placed inside the vacuum chamber. This is done to avoid possible ionization defocusing and preventing the main peak of the pulse to propagate through an underdense air plasma. The vacuum pressure in which the experiments were conducted was about 0.1mbar.

3.3 Target

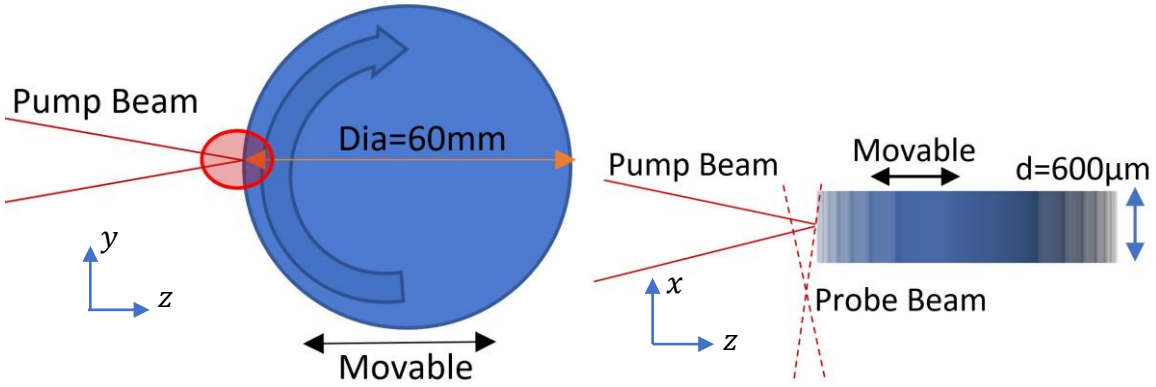

Figure 22: The target geometry depicted from the side (left image) and from the top (right image) along with the pump and probe pulse.

The target that was used in this work was an Aluminum wheel. The scale lengths of the plasma formed by fs pulses are in the range of µm, thus the probe beam needs to gain access to the exact point of plasma creation on the target. This requires the use of curved targets so that the probe can travel at grazing incidence without hitting the edges of the target in the tangential direction. Such wires require precise x-y-z target positioning system for alignment. The vacuum chamber used in this work was small and thus translational motorized stages were not able to fit inside. Thus, an Aluminum wheel shown in Figure 22 was used. This wheel target is flat in the direction of the probe beam and the probe beam is unable to gain access to the exact point of plasma creation. Therefore, the plasma is probed at later timesteps to get plasma with greater extension in the direction of the pump pulse that can be reliably scene by the tangential probe beam. The wheel has two motorized degrees of freedom, a rotation and a translation in the direction of the pump pulse. The translational movement is used to align the target within the Rayleigh length of the pump pulse while the rotational movement is used to get a fresh spot for each subsequent shot.

4 Phase Analysis from Interferograms

The previous sections discussed the theoretical concepts as well as the experimental setup utilized to carry out this work. One of the core components of this work is the interferometer, which gives access to the phase information of the probe beam. The phase of the probe is of utmost importance since it indicates the amount of the refractive index change imprinted on it by the plasma. The 3-dimensional refractive index of the plasma is in turn related to the 3-dimensional electron density as shown in equation 29. This section discusses the theoretical as well programming concepts utilized in extracting the phase information from a given interferogram.

4.1 Probe Beam Phase and Electron Density

An interferogram consists of fringes shown in Figure 23, which is a periodic pattern of bright and dark regions denoting regions of constructive and destructive interference between two beams.

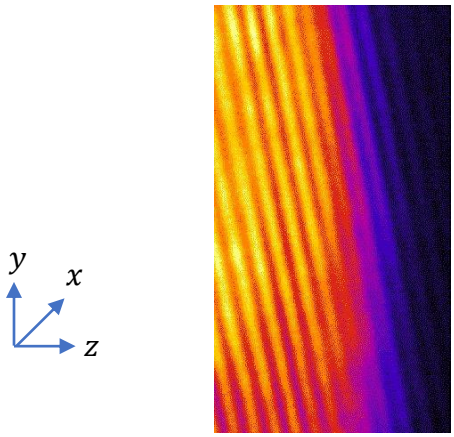

Figure 23: An interferogram without the plasma showing the fringes obtained with this experimental setup.

The detector, in this case a CCD, is relatively slow compared to the electric field and thus, gives only the intensity (averaging “fast” Electric field squared) given by equation 12:

$$I(y,z) = \langle \overrightarrow{E_1^2} \rangle (y,z) + \langle \overrightarrow{E_2^2} \rangle (y,z) + \overrightarrow{E_{01}}.\overrightarrow{E_{02}} \cos \varphi(y,z) \tag{37}$$

The last term in equation 37 contains the phase information but since cosine is a 2π-periodic function the phase is wrapped. In this work a CCD receives a 2D-image of the intensity implying a 2D phase information. The phase accumulated for the probe beam, assuming it is propagating in z-direction with the main pump propagating in x-direction, passing through an arbitrary medium is given by [42]

$$\varphi(y_j) = \int k(y_j, z).dz, \tag{38}$$

where y_j indicates the height of a ray accumulating a phase $\varphi(y_j)$ and j runs from 1 to the total number of pixels on the CCD. Any changes in the refraction of the probe beam along its path would imprint a phase on it, which can lead to errors when interpreting the interferogram. To avoid these sources of errors and restrict equation 38 to only get the phase from the region of plasma length, a reference interferogram, without the plasma, is taken. Subtracting this reference phase $\varphi_{ref} = \int k_0.dl$ from the phase with the plasma, omitting the dependences on spatial coordinates, gives

$$\Delta\varphi = \varphi_{plasma} - \varphi_{ref} = \int (k_{plasma} - k_0) dz = \int \frac{\omega}{c} (\eta - 1) dz. \tag{39}$$

Using equation 29 for the refractive index of the plasma gives

$$\Delta\varphi(y_j) = \frac{\omega}{c} \int \left(\sqrt{1 - \frac{n_e(y,z)}{n_c}} - 1 \right) dz, \tag{40}$$

where for each height y_j phase information in the z direction is averaged. The above equation can be simplified for the case where $n_e \ll n_c$ and the expression under the root can be Taylor expanded to yield

$$\eta \approx 1 - \frac{n_e(y,z)}{2.n_c}. \tag{41}$$

Then equation 40 becomes

$$\Delta\varphi(y_j) \approx -\frac{\omega}{2cn_c}\int n_e(y,z).dz \quad (42)$$

The assumption $n_e \ll n_c$ made in arriving at this relation is valid for the interferograms generated in this work, because when n_e approaches n_c the probe pulse starts deflecting, resulting in loss of transmitted power from the plasma and the visibility of the fringes reduces. Another thing of importance already noted before is that the phase information received is averaged in the z-direction. The phase information received by the CCD at the end is averaged in the z-direction but can be calculated under the assumption of a cylindrically symmetrical (around the pump beam propagation axis) plasma using Abel inversion.

4.2 Phase Extraction from Interferograms and Unwrapping

To extract the phase information from the interferogram a custom made LABVIEW program and IDEA software from Technical University of Graz was used [43]. The following is an example analysis performed on an interferogram obtained in this work. Figure 24 represents the two images used for this example analysis: the left image shows the reference, with the plasma beam blocked to remove the effect of interferometer phase errors (due to unevenness of the surfaces of the optical elements, imperfect alignment, uneven phase front of the probe pulse) and the right image shows the plasma.

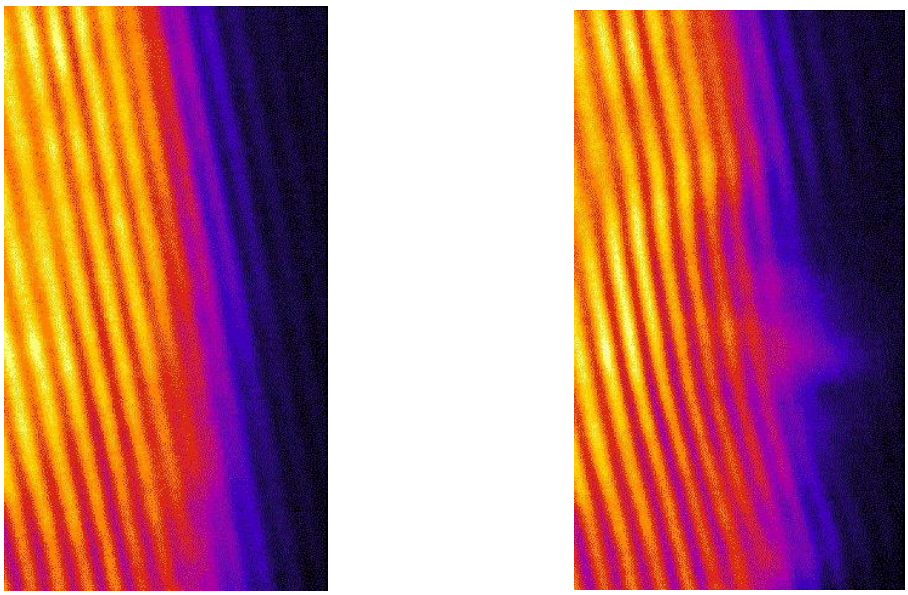

Figure 24: The diagram on the left shows a reference image (without plasma) where the fringes are straight lines. On the right is the image with bent fringes (due to plasma).

Equation 37 can be represented in a more simplified form using two general functions $a(\vec{r})$ and $b(\vec{r})$ as

$$I(\vec{r}) = a(\vec{r}) + b(\vec{r})\cos(2\pi\overrightarrow{f_0}.\vec{r} + \varphi(\vec{r})) \tag{43}$$

where $a(\vec{r})$ is the background due to the unmodulated intensity contributed by both of the fields, $b(\vec{r})$ is the modulation index, which depicts the visibility of the fringes seen on the detector and $\varphi(\vec{r})$ is the phase information that is required in this case [44]. The spatial carrier frequency is represented here by f_0. The above equation 43 can be written in the form of complex exponentials by using a function $c(\vec{r})$ defined as

$$c(\vec{r}) = \frac{1}{2}b(\vec{r})\exp(i\varphi(\vec{r})) \tag{44}$$

using which equation 43 can be written as

$$I(\vec{r}) = a(\vec{r}) + c(\vec{r})\exp(2\pi i\overrightarrow{f_0}.\vec{r}) + c^*(\vec{r})\exp(-2\pi i\overrightarrow{f_0}.\vec{r}) \tag{45}$$

where $c^*(\vec{r})$ is the complex conjugate of $c(\vec{r})$ defined in 44. Equation 45 can now be Fourier-transformed to yield the different frequencies contained in the signal detected by the CCD.

$$\tilde{I}(\vec{f}) = \tilde{a}(\vec{f}) + \tilde{c}(\vec{f} - \overrightarrow{f_0}) + \tilde{c}^*(\vec{f} + \overrightarrow{f_0}) \tag{46}$$

From the above equation it can be seen that the DC-or zero frequency contains the background while the phase information is contained around the carrier frequency $\overrightarrow{f_0}$. If the carrier frequency is high enough the phase information in the Fourier domain can be recovered. The carrier frequency depends on the fringe spacing, which can be made smaller to result in higher values of the carrier frequency. The phase information can be attained by applying a suitable mask in the Fourier domain, shifting to zero frequency and inverse Fourier transforming to get equation 44. These steps are shown in Figure 25 with the interferogram, its Fourier transformed image and inverse Fourier transformed image after applying a frequency mask.

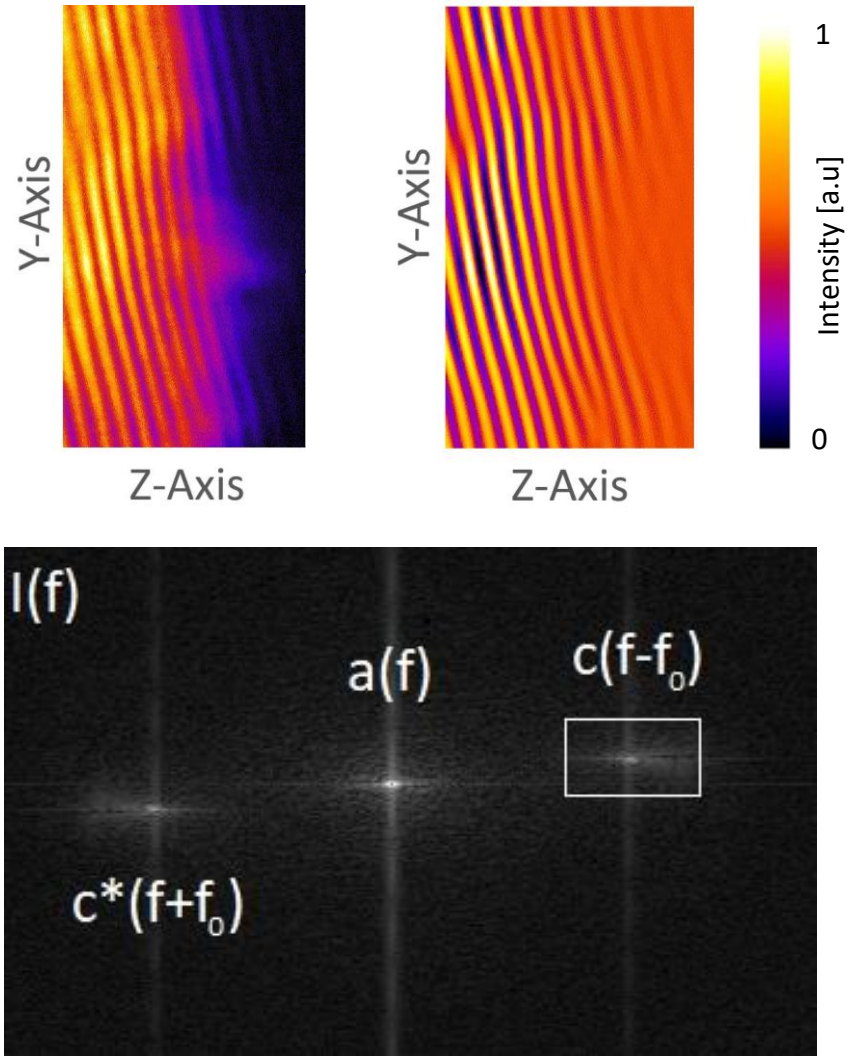

Figure 25: On the top left is the Interferogram with a plasma at the right side (The fringes are bending towards left). In the bottom is the Fourier Transform of the Interferogram with the different Fourier components and a possible mask to separate the Fourier term containing the plasma phase information. At the top right is the inverse Fourier-transform of the bottom image after applying the mask, to get only the plasma information. The intensity on the color scale is given in arbitrary units.

Taking the phase of equation 44 (and of the bottom image in Figure 25) results in the required phase information from the plasma.

Since the cosine is a 2π-periodic function, giving values between $-\pi$ and π, a step function is needed to make the discontinuous phase ϕ_d continuous. This is done by adding a step function to the discontinuous phase yielding a continuous phase ϕ_c

$$\phi_c(x,y) = \phi_o(x,y) + \phi_d(x,y) \tag{47}$$

The step function $\phi_o(x,y)$ is calculated in the program by monitoring the adjacent value in the array containing the wrapped phase information and detecting a change of 2π. If the wrapped phase is contained in an array of size, N then the step function is calculated as [45]

$$\phi_o[i] = \begin{cases} -\left\lfloor \frac{\phi_d[i]-\phi_d[i-1]}{2\pi} + 0.5 \right\rfloor * 2\pi & i = 1, \dots, N-1 \\ 0 & i = 0 \end{cases} \quad (48)$$

Since this is a 1D unwrapping, it can be performed on a 2D data set by being performed on each row of the data separately resulting in a 2D unwrapped phase. A simple case of such a phase unwrapping is shown in Figure 26. One important factor that can have an impact on the accuracy

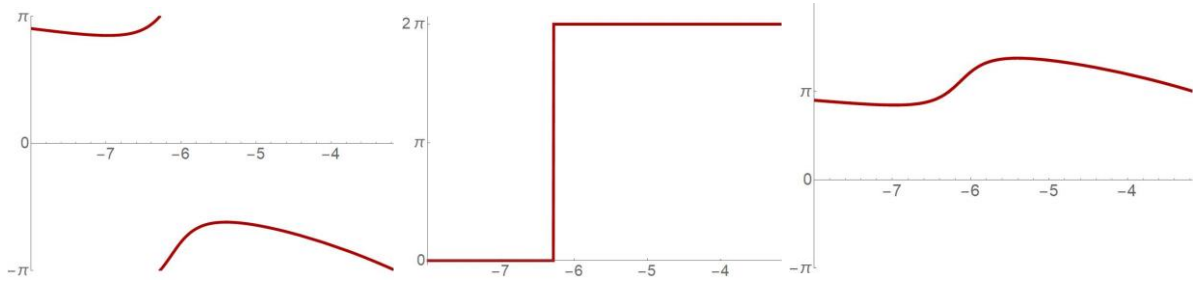

Figure 26: A simple case of unwrapping a phase. The top image shows a wrapped phase with a discontinuity. A corresponding step function is calculated from this data which has the form shown in the center image. This function is then added to the top image to get the bottom image which is continuous.

of the phase information retrieved by this Fourier analysis is the influence of the mask size used in the Fourier domain to separate the phase information from the background. Figure 27 shows an original interferogram along with three inverse Fourier transformed images taken after masking the background terms in Fourier domain. In Figure 27b the fringes are clearer than in the original interferogram due to the removal of background zero frequency term but the fringes are not bent to an extent as in Figure 27a. This is because the size of the mask 22x17 pixels is insufficient to capture all the phase information resulting in loss of information and straightening of the fringes. In Figure 27c a bigger mask of 88x40 pixels was used, which improves the amount of the phase information being captured. In Figure 27d) a bandpass filter with a size of 40 pixels was used which takes in all of the phase information but also results in background noise as can

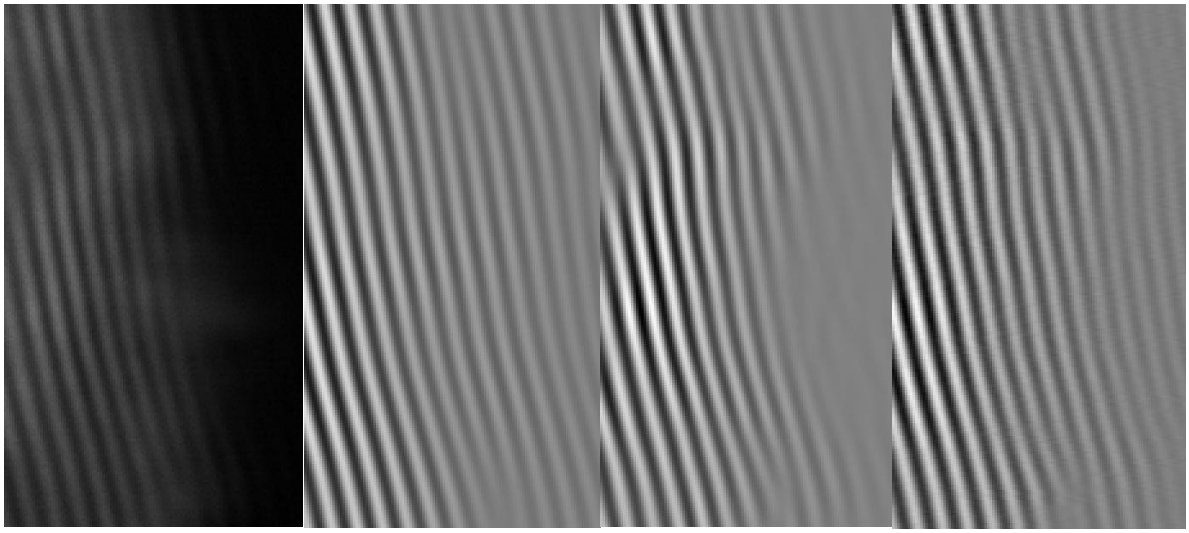

a) b) c) d)

Figure 27: The influence of the mask size on the quality of inverse Fourier transformed images: a) represents the original interferogram, b) inverse Fourier with a rectangular mask of size 22x17pixels, c) inverse Fourier with a rectangular mask of size 88x40 pixels, d) inverse Fourier with a band pass filter of 40 pixels.

be clearly seen in the figure above. This implies a trade-off between the amount of noise and amount of phase information, which was studied in more detail in the work of Jens Polz [46]. In this work the data was taken with a bandpass mask with a size of 40 pixels corresponding to a size of 11 µm, which does results in noise but gives the best result for the plasma phase information.

4.3 Plasma Density via Abel Inversion

The above Fourier analysis is performed on both the reference image (without plasma) and on the image with the plasma and subtracted at the end to yield phase information from the plasma only. The next step in the phase analysis is getting a 3D phase information from the averaged data. Under cylindrical symmetry the Abel inversion integral can be applied on the 2D phase to gain access to the electron density of the plasma.

4.3.1 Analytical Abel Inversion

The relation between the probe beam phase and the electron density of the plasma was derived and given in equation 42

$$\Delta\varphi(y_j, z) \approx -\frac{\omega}{2cn_c}\int n_e(x, y_j, z)dx \tag{49}$$

This equation can then be given converted into cylindrical coordinates by substituting $\rho = x^2 + y^2$ giving $dx = \frac{d\rho}{\sqrt{\rho^2 - y^2}}$.

$$\Delta\varphi(y, z) \approx -\frac{\omega}{cn_c}\int_y^R n_e(\rho, z)\ \frac{\rho d\rho}{\sqrt{\rho^2 - y^2}} \tag{50}$$

This is known as the Abel Transform, which relates a symmetrical function with its chord integrals (integrals along an axis). Since the quantity of interest here is $n_e(x, y, z)$, the inverse Abel Transform can be used given as [47]

$$n_e(\rho, z) = -\frac{\lambda_L n_c}{\pi}\int_r^R \frac{d}{dy}\Delta\varphi(y, z)\frac{dy}{\sqrt{y^2 - \rho^2}} \tag{51}$$

The above equation needs to be solved numerically to yield the electron density in the plasma. When the CCD camera records the interferogram, it samples the continuous light distribution into a discrete set of values recorded by the individual pixels. Thus, the data is available in a digitized form requiring the Abel inversion to also be performed in a discrete manner. Different numerical methods are used to perform the discrete Abel inversion [48].

4.3.2 Discrete Abel Inversion

Equation 51 can be solved using numerical methods to compute the derivatives of the averaged phase information available in the interferogram. Similarly, the integration is also done using digital numerical methods that operate on digitized arrays. The differentiation is performed using a method known as "2nd order central" that approximates the derivative as [49]

$$D_{y_j} = \Delta\varphi\frac{d}{dy}\Delta\varphi[y, z]\Big|_{y_j} = \frac{1}{2}(\Delta\varphi[y_{j+1}, z] - \Delta\varphi[y_{j-1}, z]). \tag{52}$$

Here $\Delta\varphi[y_{j+1}, z]$ represents the value of the phase information at the position $j + 1$ in the array containing the discrete values of phase. The integral is performed numerically by the trapezoidal rule given as [49]

$$n_{e1}(\rho,z) = -\frac{\lambda_L n_c}{\pi}\sum_{i=1}^{N-1}\frac{1}{2}\left(D_{y_j}.\frac{1}{\sqrt{{y_j}^2-\rho^2}} + D_{y_{j+1}}.\frac{1}{\sqrt{{y_{j+1}}^2-\rho^2}}\right) \quad (53)$$

where N represents the size of the array. These numerical methods give the electron density in units of $\mathrm{cm}^{-3}\mu\mathrm{m/pixel}$. To get the value of the electron density in the usual units of cm^{-3}, an appropriate magnification factor M that depends on the imaging optics and the camera properties must be used. The final electron density in units of cm^{-3} is given as

$$n_e(\rho,z) = \frac{n_{e1}(\rho,z)}{M} \quad (54)$$

4.4 Interferogram to Scale Lengths

As described in the previous section, a reference interferogram was taken with each shot of plasma to isolate the phase contributions from plasma. To outline the procedure of plasma scale lengths from raw interferograms an example is shown in Figure 28. The dark area

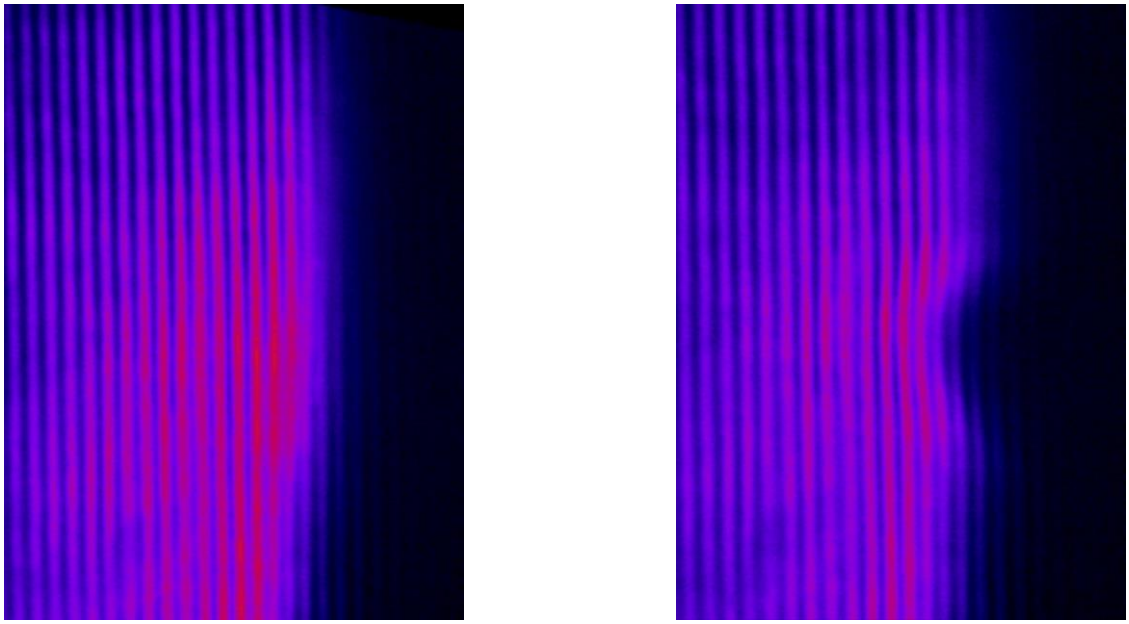

Figure 28: An example interferogram with a reference image (without the plasma) on the left and with plasma on the right. Note that the dark area on the right is the aluminum wheel.

on the right of each image is the aluminum wheel surface. The bent fringes in the middle are due to the phase disturbance resulting from the pump-pulse generated plasma. These interferograms were then analyzed by Fourier transforming and isolating the frequency component containing the phase. The 2D phase obtained from the interferogram is shown in Figure 29. Since the plasma

electron density relates directly to the 3-D phase, the need for Abel inversion arises. Under cylindrical symmetry the discrete Abel inversion is applied, and the result is shown in Figure 30.

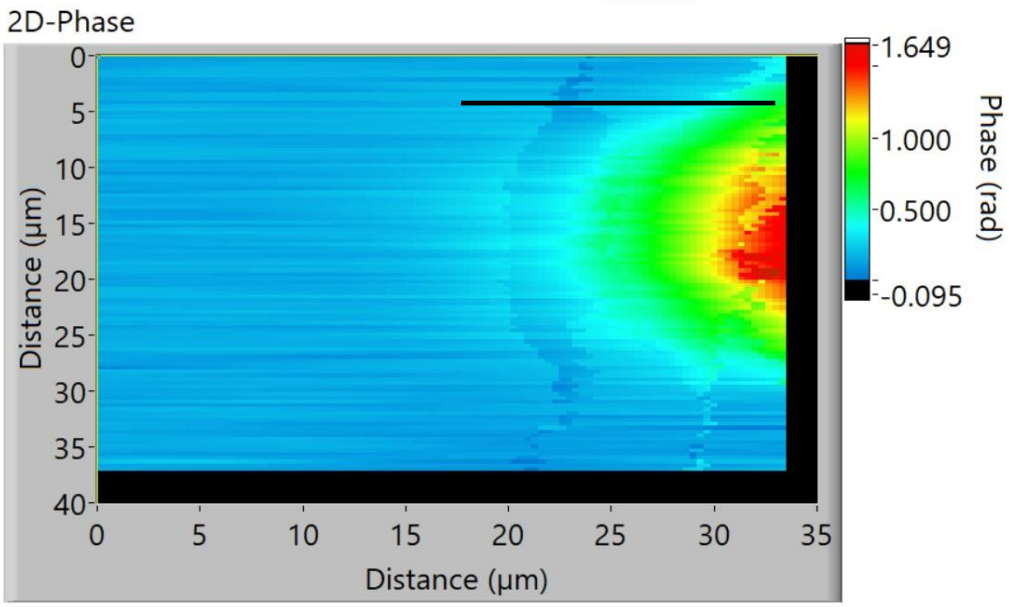

Figure 29: The 2D phase obtained by analyzing the interferograms.

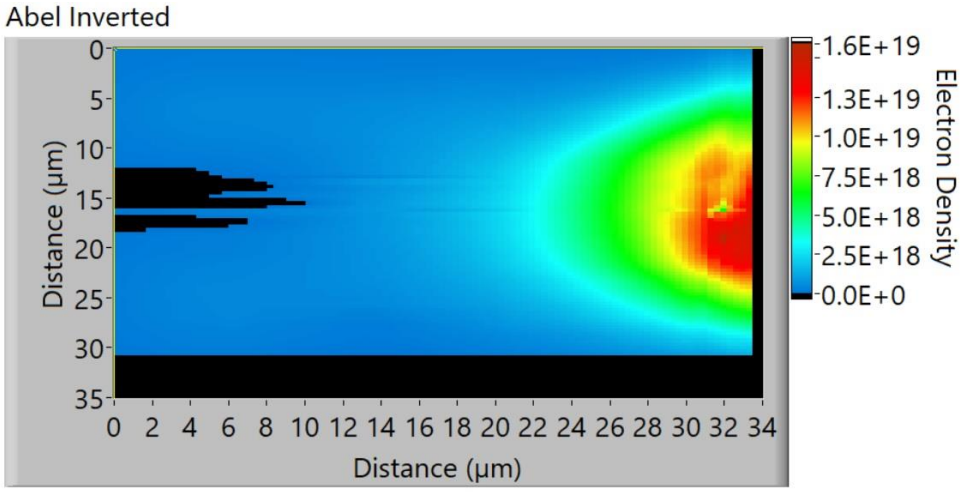

Figure 30: Abel inverted data to yield plasma electron density profile. This is a cutout from the 3D electron density profile at the plane in the center of the plasma.

The Electron density profiles attained from the Abel inversion were then used to calculate the plasma scale lengths and the plasma electron temperatures. The black line depicts the position where a lineout of this 2-D data is taken to get the plasma density values along a line. A log of this data is then taken to generate a linear data shown in Figure 31 and a fit is made to calculate

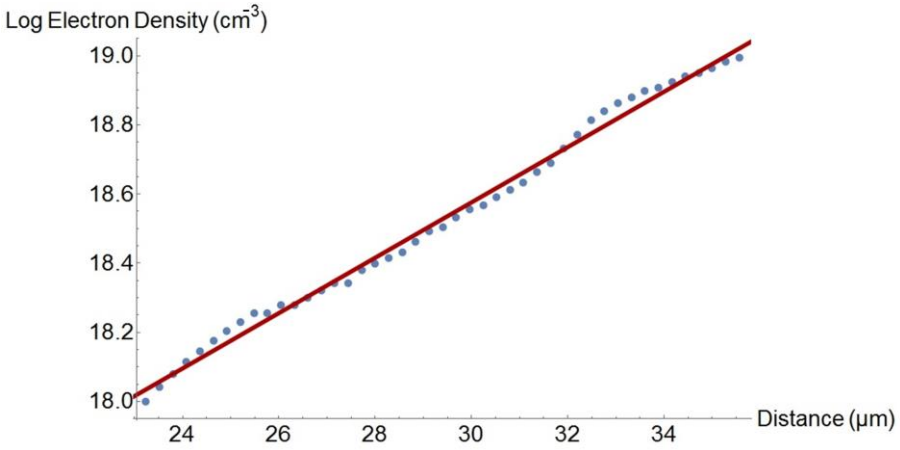

Figure 31: The log electron density raw data with a linear fit use to calculate the plasma electron density scale length. The data is restricted from 18 to 20 on the log scale.

the electron density scale length. The log of an exponential profile yields

$$Log_{10}\left[e^{-\frac{x}{L}}\right] = -0.43\frac{x}{L} = mx \tag{55}$$

where m is calculated from the fit and then used to yield plasma scale length L. In this work, MULTI-fs simulations [50] for the intensities used in this experiment were also attained and compared with the experimental values. A similar fit to the plasma electron density log profiles attained from the simulation was computed to get the plasma scale lengths. The data from the simulation as well as the experiment was restricted to a certain range to avoid errors and noise. The minimum detectable phase of the interferometer was 0.15 rad that corresponds to a minimum detectable electron density of 10^{18} cm^{-3}. The minimum limit is determined by the amount of the data captured by the frequency mask. A larger mask captures more frequency information but is ultimately limited due to the noise from other frequency components. Increasing the fringe number can result in a larger separation between the frequency components and thus, less cross over noise from other frequencies. This can also only be done to a certain limit, as increasing the fringe number, decreases the pixels per fringe resulting in the CCD being unable to detect fringes.

The critical density for the probe laser being used in this work was 10^{21} cm^{-3} but the probe laser deflects out of the collecting objective when the plasma density reaches 10^{20} cm^{-3}. Thus, the simulation and the experimental data was analyzed between this range of electron densities only. The experimental setup yields two different time steps in a single shot that can give access to

plasma velocity as well. This was used to calculate the plasma electron temperature using the equation

$$c_s \approx 3.1 \times 10^7 \left(\frac{T_e}{keV}\right)^{\frac{1}{2}} \left(\frac{Z^*}{A}\right)^{\frac{1}{2}} cm\, s^{-1} \quad (56)$$

where T_e is the electron temperature, Z^* is the ionization number, A is the atomic number and c_s is the plasma blow-off velocity. The ionization degree was calculated from equation 20, where the different ionization mechanisms were considered. The velocity was calculated from the single shot probing through the difference of scale lengths at different times and then equation 56 was used to result in plasma electron temperatures.

5 Results

In this section, the results obtained are presented and discussed in the context of different absorption processes. The Abel inversion was applied using a custom made LABVIEW program and follows the discrete Abel inversion equation derived in the previous section. The section starts with the results of an energy as well as a time scan done using a linearly polarized pump pulse. The possible reasons for the results are then discussed and corroborated from the literature. Then the results of the plasma scale lengths using a circularly polarized pump pulse are presented. The two different polarizations were used to get an insight into the different processes dominating the laser absorption into the plasma.

5.1 Linearly Polarized Pump Pulse

A linearly polarized pump pulse described in section 3.2 was used to generate plasma from aluminum wheel target. Each of the scale length in this section was averaged over 2 or 3 shots. First a time scan was performed with a pump pulse intensity of 1.9 x 10^{16} W/cm^2, where one of the pulses was kept fixed at 46ps after the creation of the plasma and the other pulse was delayed from 21 - 48ps. The zero delay of the pump and the probe was characterized by decreasing the delay and observing the phase changes in the probe beam. When the phase was no longer detectable with the interferometer (minimum detectable phase ≈ 0.15), this point was assumed to be the zero delay. The plasma scale lengths for each time was analyzed and the results are presented in Figure 32. The plasma scale lengths vary from 4.2 to about 10.5 µm, implying a sufficient spatial resolution of 3.5 µm of the probe pulse to probe these plasmas. The general trend of the plasma scale lengths is an increase as the time is increased, which is expected since at later times the plasma has expanded more resulting in a larger plasma scale length.

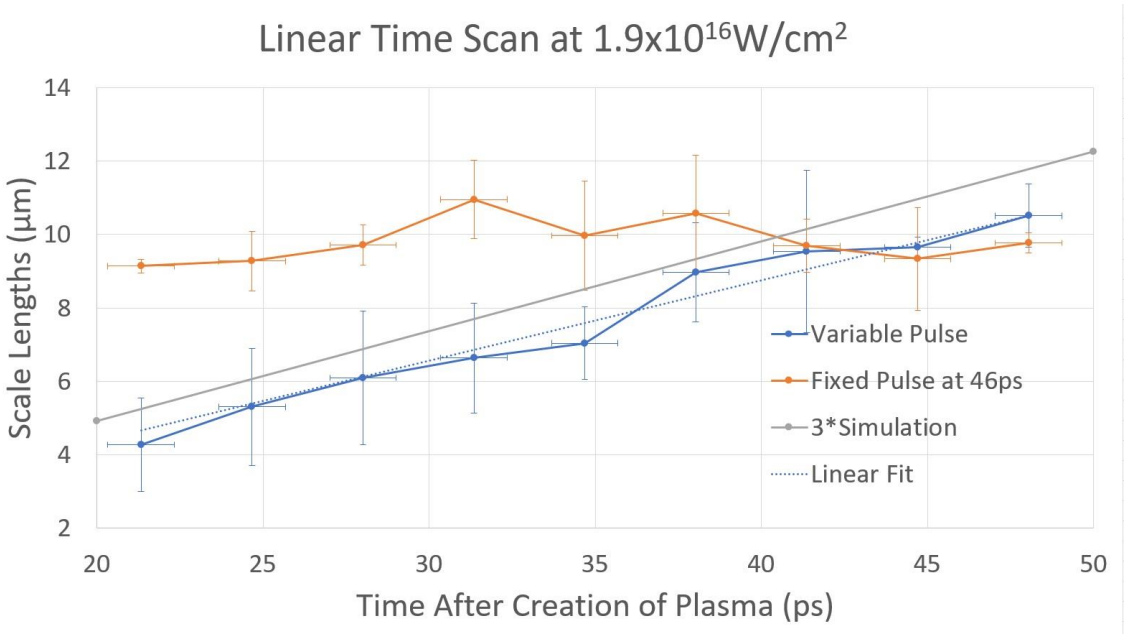

Figure 32: The scale lengths vs the time after creation of the plasma for a linearly polarized pump pulse with one of the probe pulses being delayed (blue) and the other kept fixed (orange).

The simulation data is obtained by analyzing the MULTI-fs simulation in a similar fashion as that described for the experimental data. The errors in the measurement of the scale lengths mainly arise due to fluctuations among the shots, due to unstable energy output of the source regenerative amplifier. In addition, there are errors associated with the analysis when a fit is done on the log data to calculate the plasma scale lengths. The errors in the time is due to the jitter between the pump and the probe that arises because of slight changes in the propagation lengths due to vibrations of the optical elements (lens, mirrors, etc.). If the laser pulse has a slightly different direction, compared to the previous one, it moves in a slightly different path resulting in different times. The simulation data has been multiplied by 3 and then plotted on top of the measured data, since the scale lengths predicted by simulation are 3 times smaller than those measured with the setup. Both the measured and the simulated data have a zero intercept on this graph indicating that the absence of plasma before the main pump pulse has hit the target. Afterwards, the measured scale lengths increase three times faster than the simulated scale lengths.

A possible explanation for a faster increase in the measured scale lengths can be attained when the absorption mechanisms are considered. A higher absorption than that predicted by the simulation can result in a faster increase of scale lengths after the pump pulse, since a higher absorbed fraction can result in higher electron temperatures that in turn leads to faster

expansion of the plasma. In the MULTI-fs [50] hydrodynamic expansion code, two major absorption mechanisms have been taken into account. The collisional absorption is the main process that is present in the code, since up to 10^{15} W/cm^2 the absorption physics is dominated by collisional processes. Another process that is present in the code is the resonant absorption, which is not considered explicitly but implicitly while solving for wave equations. The solution for the p-polarized wave already gives rise to Langmuir waves inside the plasma and thus resonance absorption is also catered for, in the hydrodynamic code. In the case of this work, the resonance absorption and vacuum heating is expected to be minimal, since the beam was normally incident on the target. This is also later confirmed when a circularly polarized pump pulse is hit on the target resulting in the same scale lengths. Thus, to explain the faster increase of scale lengths in the measured data, different skin effects under normal incidence are considered such as Anomalous Skin effect (ASE), not explicitly taken into account in the hydrodynamic code. To consider the extent of this effect, the work of Rozmus and Tikhonchuk [51] was analyzed, where they presented an analytical model of normal and anomalous skin effect with step like density profiles such as those expected in this work, because of fs-pulses. The absorption percentage due to NSE shown (curve 1) and ASE (curve 2) is shown in Figure 33 [51]. This absorption is

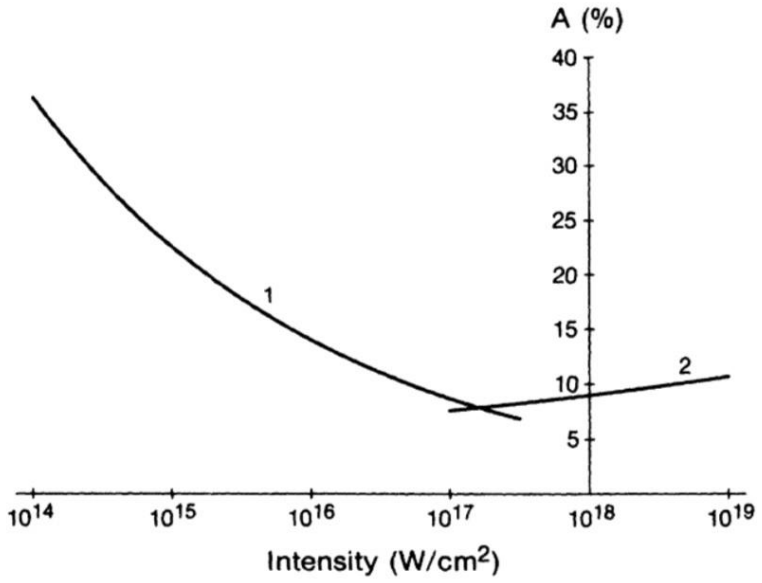

Figure 33: The absorption coefficient for Normal Skin Effect (NSE) curve 1 and Anomalous Skin Effect (ASE) curve 2 as a function of intensity for pulses with a central wavelength of 250nm with aluminum targets under normal incidence [51].

calculated for a laser pulse with a central wavelength of 250nm under normal incidence with aluminum targets. Curve 2 starts to shift towards the left and contributes more at lower

intensities when the central wavelength of the pump pulse is increased. This is due to the fact that the electron mean free path increases as the laser wavelength is increased since it is accelerated by the Electric field in one direction for a longer period of time as opposed to a laser with high frequency (lower wavelength). A larger mean free path of the electron results in a greater Anomalous skin effect. A contribution from the ASE can then increase the electron temperature and result in faster expansion of the plasma electron density. The model also predicts a plasma electron temperature of 200eV for pulse durations of 120fs at an intensity of 10^{15} W/cm^2 for aluminum targets as shown in Figure 34 [51]. The experimental temperature determined using the plasma velocity is 262eV that is close to the value predicted by the model. The slightly higher value can be attributed to the higher intensity pulse ($1.9\text{x}10^{16}$ W/cm^2) with which the plasma was created in this work than the value used in

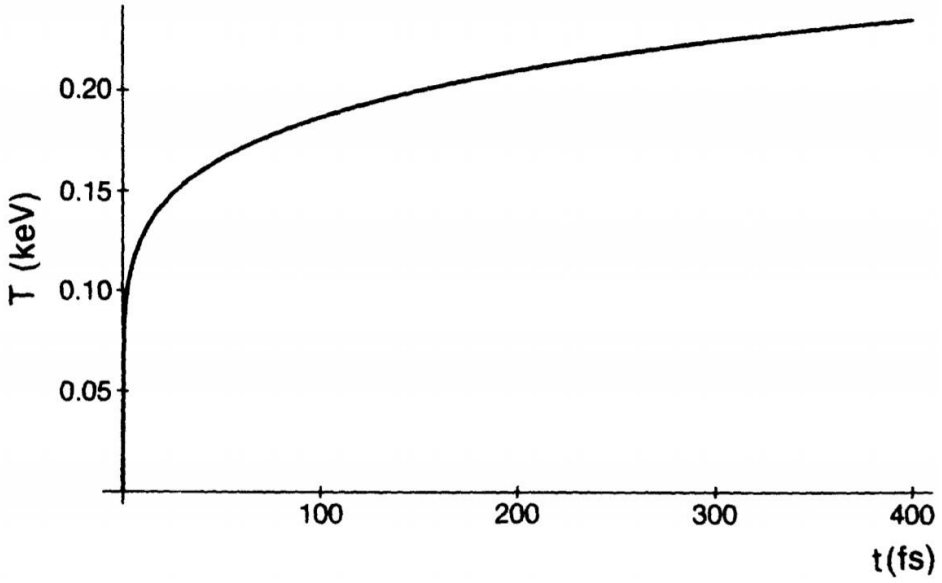

Figure 34: The temperature as a function of the pulse duration under normal incidence for an intensity of 10^{15} W/cm^2 as predicted by the model of Rozmus [51].

the model. This model also correctly predicts the temperature values for the experimental work of Fedosejevs et.al, which found experimental temperature values of 310eV at $2.5\text{x}10^{15}$ W/cm^2 for 150-fs pulses at wavelength of 250nm [52]. These values differ from the current work due to lower intensity and a lower wavelength.

After the time scan an intensity scan ($0.67\text{-}3\text{x}10^{16}$ W/cm^2) was conducted done using the linearly polarized laser pulse and the results are shown in Figure 35 where the simulation graph is again multiplied by 3 but is taken at a time of 50ps. The two probe pulses are kept fixed at

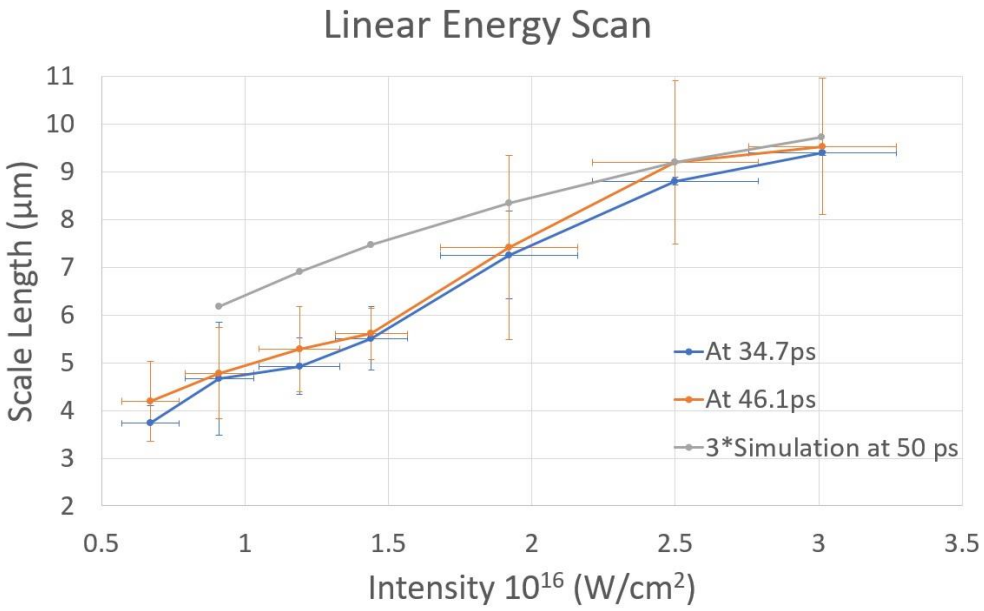

Figure 35: The scale lengths vs intensity (0.67-3x10^{16} W/cm^2) for a linearly polarized pump pulse with both pulses fixed at different times, one at 34.7ps (blue) and the other at 46.1ps (orange).

different time steps, one at 34.7 ps and the other at 46.1ps after the creation of the plasma. The general trend in the intensity scan is an increase of plasma scale lengths, which can be attributed to an increase in total absorption. The plasma electron temperature cannot be determined reliably here due to larger error bars. The mismatch between the simulated and the measured data can be attributed to the contribution of the ASE as determined using the analytical model discussed previously.

5.2 Circularly Polarized Pump Pulse

After the linearly polarized pump pulse described in the experimental setup, a circularly polarized pump pulse having E-field components in two orthogonal directions was also used to generate plasmas. The circular polarization was generated using a quarter lambda waveplate. For the circularly polarized pump pulse no simulated data was available and thus it can be compared with the data from the linearly polarized pump pulse to detect any changes in the plasma electron temperature and scale lengths. A time scan was first done an intensity of 1.9 x 10^{16} W/cm^2 where

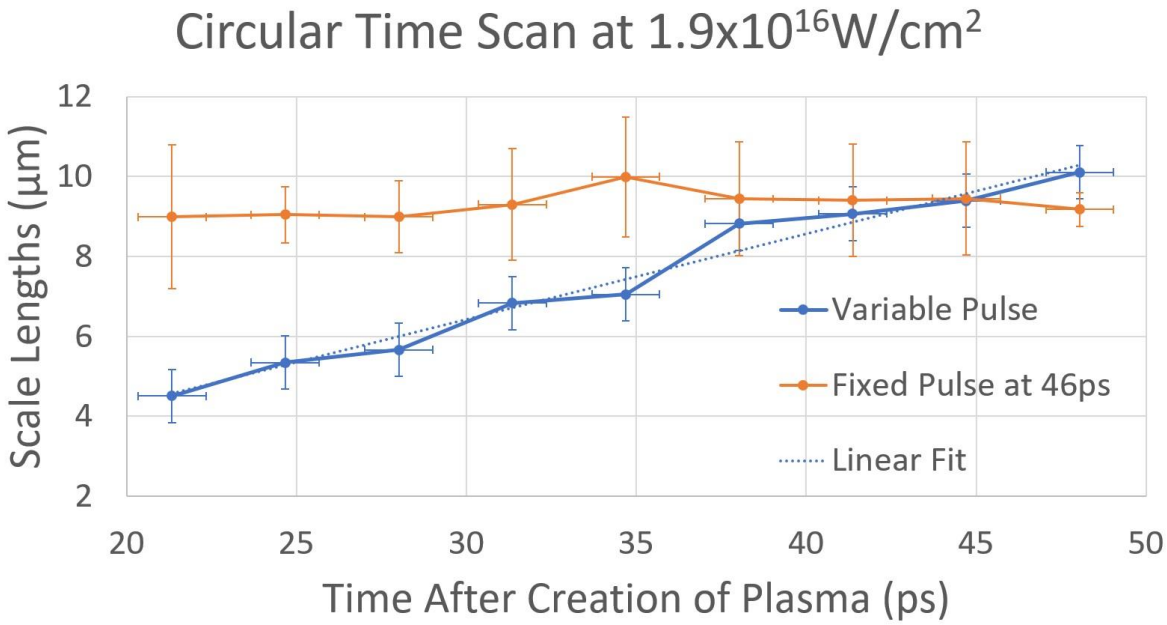

Figure 36: The time scan for a circularly polarized pump pulse at an intensity of 1.9x1016 W/cm2 with one of the probe pulses varied from 21-48 ps (blue) and the other kept fixed at 46 ps (orange).

one of the pulses was kept fixed at 46ps after the creation of the plasma and the other pulse was delayed from 21 - 48ps. The results are presented in Figure 36. Here again the plasma scale lengths increase with time because of the plasma expansion. The plasma scale lengths vary from 4.3 to about 10 µm similar to the results obtained from linearly polarized pump pulse. This can be attributed to the fact that the absorption physics for both the circularly polarized laser pulse and the linearly polarized laser pulse is the same. Two of the mechanisms, resonance absorption and vacuum heating, rely on the presence of the p-polarized laser pulse. The plasma temperature for the linearly polarized laser pulse (262eV) and the temperature for circularly polarized laser pulse (241eV) are similar, implying minimal contribution to total absorption from resonance absorption or vacuum heating. Resonance absorption is more dominant under a larger degree of incidence angle [21], which is not the case here due to normal incidence. Vacuum heating under normal incidence is also negligible [21] having an absorption percentage of only 1% under 10°. Thus, for both circularly and linearly polarized pump pulse the dominant absorption processes are the collisional absorption under the normal and anomalous skin effect.

A similar intensity scan for a circular polarized pump pulse was also conducted to study its behavior and the results are shown in Figure 37. The resulting plasma scale lengths increase as

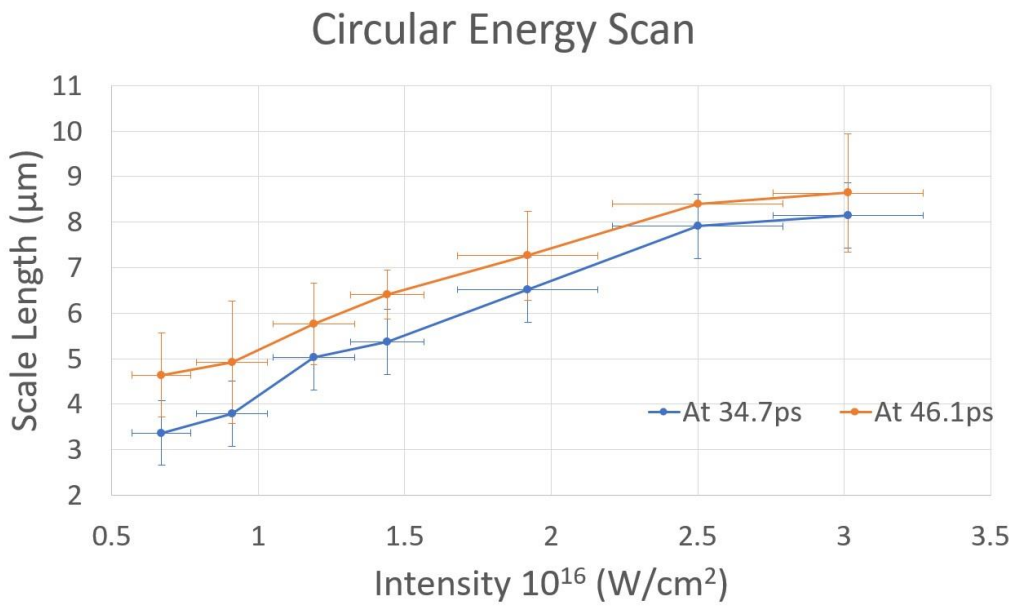

Figure 37: The intensity scan from 0.67-3x1016 W/cm2 with one of the pulses kept fixed at 34.7ps and the other kept fixed at 46.1ps. The intensity was changed by varying the energy from the regenerative amplifier.

the intensity increases implying a constant absorption factor. The absorption factor due to collisional absorption factor from Figure 33 is shown to decrease, thus a near constant absorption factor here can be attributed to a contribution from the ASE. Since the error bars of the plasma scale lengths are large the temperature cannot be reliably determined for this case. This is an area, where further experiments can be conducted to result in reduction of error in the plasma scale lengths. This can then be used to result in more precise electron temperatures.

In this work, the characterization of the plasma was completed for the case of different intensity and polarization states of the pump pulse. A comparison with literature values was drawn and dominant absorption processes were identified to be normal and anomalous skin effects. This setup can further advance the knowledge of the pre-plasma environment created in the TNSA process before the main pulse arrives.

6 Conclusion and Outlook

TNSA process is an important means to generate energetic ion beams. The understanding of the pre-plasma is an important step towards optimizing the TNSA process. In this work, a complete system to generate and characterize different kinds of plasma was assembled. Generating two pulses and using them to probe the plasma in a single shot increases the utility of such a step since it eliminates the shot to shot variations. Different absorption mechanisms were considered while investigating the plasma and their dominance evaluated in the context of current work.

Two devices named temporal separation and spatial separation devices were used to generate the probe pulses. An imaging system to focus, collect and relay the pulses at a large distance was built and optimized to generate near diffraction limited spatial resolution (≈3.5µm). The pulses also give a sufficient temporal resolution with 330 fs pulses to study the hydrodynamic evolution of the plasma. The plasma was created with pulses ranging in intensity from 0.67×10^{16} to 3×10^{16} W/cm^2 with a pulse duration of 120 fs at a central wavelength of 1.03 µm. An intensity as well as a time scan was done to evaluate the plasma based on the scale lengths and plasma electron temperature. Both linear and circular polarization of pump pulse was used to create the plasma. A custom LABVIEW program was used to analyze the phase and generate scale lengths from it by Fourier transform. To gain access to the 3-D information, a cylindrical symmetry was assumed, and Abel inversion was applied on the 2-D chord phase integrals. From this, plasma scale lengths were calculated, and utilizing the single-shot pulses at different time steps, plasma velocity and plasma electron temperatures were calculated.

Both the linear and circular polarized pump pulses generated plasma scale lengths in the range of 4-10 µm with an electron temperature of 50-280 eV. This data was also compared with MULTI-fs simulation data and possible reasons of deviations discussed. Dominant absorption mechanisms identified are the Normal and Anomalous Skin Effects under normal incidence. The similarity in the plasma scale lengths and the plasma electron temperature for both polarization implies the absence of vacuum heating and resonance absorption. This is also confirmed by

underlying physics of these two absorption processes, which require an electric field component in the direction of the plasma electron gradients.

The system now can be used for a detailed study by changing pump pulse parameters such as incidence angles, intensity range etc. It is a complete system with the ability to generate as well as probe and study different plasmas with a 1Hz repetition rate. This study can then be used to optimize the laser-plasma energy coupling and consequently approach the TNSA process with a new perspective. The probing setup also has the possibility to increase the number of pulses currently used by generating a broader bandwidth and cutting the spectrum with more mirrors. This approach would result in single-shot probing with a larger number of timesteps, which can thus reduce the error in the plasma temperature measurements. A system is currently being built to amplify a broadband source to serve as the probe source.

The investigation of the pre-plasma characteristics, discussed in this thesis, are intended to further enhance the knowledge and understanding of the plasma dynamics. An effort in this direction can prove to be fruitful to optimize TNSA process and can ultimately lead to more compact ion sources increasing their applicability.

7 References

[1] Danson, Colin, et al. “Petawatt Class Lasers Worldwide.” *High Power Laser Science and Engineering*, vol. 3, 2015, p. e3.

[2] Tajima, T., and J. M. Dawson. “Laser Electron Accelerator.” *Physical Review Letters*, vol. 43, no. 4, 1979, pp. 267–270.

[3] Macchi, Andrea, et al. “Ion Acceleration by Superintense Laser-Plasma Interaction.” *Reviews of Modern Physics*, vol. 85, no. 2, 2013, pp. 751–793.

[4] Cerchez, Mirela. “Ultrashort Laser Pulse Interaction with Overdense Plasmas.” *Mathematisch-Naturwissenschaftichen Fakultät der Heinrich-Heine-Universität Düsseldorf*, University of Dusseldorf, 2008.

[5] Amaldi, Ugo, and Gerhard Kraft. “Radiotherapy with Beams of Carbon Ions.” *Reports on Progress in Physics*, vol. 68, no. 8, 2005, pp. 1861–1882.

[6] Passoni, M., and M. Lontano. “Theory of Light-Ion Acceleration Driven by a Strong Charge Separation.” *Physical Review Letters*, vol. 101, no. 11, 2008.

[7] Nolte, Stefan. “Ultrafast Optics [Lecture Notes]”, Institute of Applied Physics, Jena, Germany.

[8] Diels, Jean-Claude, and Wolfgang Rudolph. "Fundamentals." *Ultrashort Laser Pulse Phenomena*. 2nd ed. Amsterdam: Academic, 2006. 1-4. Print.

[9] González-Velasco, Enrique. "Fourier Transforms." *Fourier Analysis and Boundary Value Problems*. San Diego, CA: Academic, 2008. 242-45. Print.

[10] Weiner, Andrew. "Introduction to Ultrashort Pulse Generation through Mode-locking." *Ultrafast Optics*. John Wiley & Sons, 2011. Print.

[11] Paschotta, Rüdiger. "Ultrashort Pulses." *Encyclopedia of Laser Physics and Technology - Semiconductor Optical Amplifiers, SOA*. RP Photonics Consulting GmbH, 30 Mar. 2017. Web. 14 Sept. 2018.

[12] Boyd, Robert W. "Wave-Equation Description of Nonlinear Optical Interactions." *Nonlinear Optics*. London: Academic, 2008. 112-14. Print.

[13] Lederer, Falk, et al. “Propagation of Gaussian beams.” *Fundamentals of Modern Optics [Lecture Script]*, Institute of Applied Physics, Jena, Germany.

[14] Saleh, Bahaa E. A., and Malvin Carl. Teich. "Wave Optics." *Fundamentals of Photonics*. Hoboken, NJ: Wiley-Interscience, 2009. Print.

[15] Gerrard, Anthony, and James M. Burch. “2 Matrix Methods in Paraxial Optics.” *Introduction to Matrix Methods in Optics*, Dover, 1994. Print

[16] Hecht, Eugene. "Interference." *Optics*. 5th ed. Boston: Pearson, 2017. 398-400. Print.

[17] Born, Max, Emil Wolf, and Avadh Behari Bhatia. *Principles of Optics Electromagnetic Theory of Propagation, Interference and Diffraction of Light*. Cambridge: Cambridge U, 2016. Print.

[18] Akcay, C., Parrein, P. & Rolland, J. P. Estimation of longitudinal resolution in optical coherence imaging. *Appl. Optics* 41(25), 5256–5262 (2002). Print.

[19] Einstein, A. "Über Einen Die Erzeugung Und Verwandlung Des Lichtes Betreffenden Heuristischen Gesichtspunkt [AdP 17, 132 (1905)]." *Annalen Der Physik* 14.S1 (2005): 164-81. Print.

[20] Hölzl, J., and F. K. Schulte. "Work Function of Metals." *Springer Tracts in Modern Physics Solid Surface Physics*(1979): 1-150. Print.

[21] Gibbon, Paul. "Interaction with Single Atoms." *Short Pulse Laser Interactions with Matter: An Introduction*. London: Imperial College, 2005. 18-22. Print.

[22] Fedorov, M. V. "L. V. Keldysh’s “Ionization in the Field of a Strong Electromagnetic Wave” and Modern Physics of Atomic Interaction with a Strong Laser Field." *Journal of Experimental and Theoretical Physics* 122.3 (2016): 449-55. Print.

[23] Lambropoulos, P. "Mechanisms for Multiple Ionization of Atoms by Strong Pulsed Lasers." *Physical Review Letters*55.20 (1985): 2141-144. Print.

[24] Oppermann, Malte. “Molecules in Strong Laser Fields.” *Resolving Strong Field Dynamics in Cation States of CO_2 via Optimised Molecular Alignment Springer Theses*, 2014, pp. 9–50.

[25] Jönsson, Lars. "Energy Shifts Due to the Ponderomotive Potential." *Journal of the Optical Society of America B* 4.9 (1987): 1422. Print.

[26] Torrisi, L., and M. Cutroneo. "Aluminium Plasma Production at High Laser Intensity." *Journal of Applied Physics*115.8 (2014): 083105. Print.

[27] Lederer, Falk, et al. “Optical fields in dispersive and isotropic media.” *Fundamentals of Modern Optics [Lecture Script]*, Institute of Applied Physics, Jena, Germany.

[28] Grosso, Giuseppe, and Giuseppe Pastori Parravicini. "Optical and Transport Properties in Metals." *Solid State Physics*. Oxford: Academic, 2014. 396-400. Print.

[29] Chen, Francis F. "Waves in Plasma." *Introduction to Plasma Physics and Controlled Fusion*. New York: Springer, 2016. 106-08. Print.

[30] Gibbon, Paul. "Interaction with Solids." *Short Pulse Laser Interactions with Matter: An Introduction*. London: Imperial College, 2005. 128-9. Print.

[31] Danson, Colin, David Hillier, Nicholas Hopps, and David Neely. "Petawatt Class Lasers Worldwide." *High Power Laser Science and Engineering* 3 (2015): Print.

[32] Sharma, Ashutosh, and Zoltán Tibai. "Ion Acceleration in Plasmas." *University in Pécs*. Hungarian ELI Project, n.d. Web. 18 Oct. 2018.

[33] Wilks, S.C., et al. “Energetic Proton Generation in Ultra-Intense Laser–Solid Interactions.” *Physics of Plasmas*, vol. 8, no. 2, 2001, pp. 542–549.

[34] Macchi, Andrea, et al. “Ion Acceleration by Superintense Laser-Plasma Interaction.” *Reviews of Modern Physics*, vol. 85, no. 2, 2013, pp. 751–793.

[35] Drake, R. P., et al. “Laser-Intensity Scaling Experiments in Long-Scalelength, Laser-Produced Plasmas.” *Physics of Fluids*, vol. 31, no. 6, 1988, pp. 1795.

[36] Ginzburg, V. L., et al. “Propagation of Electromagnetic Waves in Plasma.” *Physics Today*, vol. 15, no. 10, 1962, pp. 70–73.

[37] Brunel, F. “Not-so-Resonant, Resonant Absorption.” *Physical Review Letters*, vol. 59, no. 1, 1987, pp. 52–55.

[38] Rozmus, W., and V. T. Tikhonchuk. “Skin Effect and Interaction of Short Laser Pulses with Dense Plasmas.” *Physical Review A*, vol. 42, no. 12, 1990, pp. 7401–7412.

[39] Kruer, W. L., and Kent Estabrook. “J×B Heating by Very Intense Laser Light.” *Physics of Fluids*, vol. 28, no. 1, 1985, pp. 430–432.

[40] *Resolution Test Targets*, www.thorlabs.de/newgrouppage9.cfm?objectgroup_id=4338.

[41] “Image Formation.” *Optical Physics*, by Stephen G. Lipson et al., Cambridge Univ. Press, 2004.

[42] Hutchinson, Ian H. *Principles of Plasma Diagnostics*. Cambridge: Cambridge UP, 2005. 115-17. Print.

[43] "IDEA - Interferometric Data Evaluation Algorithms." *Idea2*. N.p., n.d. Web. 17 Sept. 2018.

[44] Takeda, Mitsuo, Hideki Ina, and Seiji Kobayashi. "Fourier-transform Method of Fringe-pattern Analysis for Computer-based Topography and Interferometry." *Journal of the Optical Society of America* 72.1 (1982): 156-60. Print.

[45] LABVIEW Help.

[46] Polz, Jens. *Zeitaufgelöste Untersuchung Der Ionenbeschleunigung Bei Relativistischen Laser-Plasma-Wechselwirkungen an Dünnen Folien*. Thesis. Friedrich Schiller University of Jena, 2008. Jena: U of Jena, 2008. Print.

[47] Gindikin, Simon. *The Legacy of Niels Henrik Abel The Abel Bicentennial, Oslo, 2002*. By Olav Arnfinn Laudal and Ragni Piene. Berlin: Springer Berlin, 2013. 585-90. Print.

[48] Hipp, Martin, and Peter Reiterer. "User Manual for IDEA 1.5." *Optics TU Graz*. N.p., July 2003. Web. 20 Sept. 2018.

[49] Atkinson, Kendall E. *An Introduction to Numerical Analysis*. New York: John Wiley & Sons, 1989. Print.

[50] Ramis, R., et al. "MULTI-Fs – A Computer Code for Laser–Plasma Interaction in the Femtosecond Regime." *Computer Physics Communications*, vol. 183, no. 3, 2012, pp. 637–655.

[51] Rozmus, W., and V. T. Tikhonchuk. "Skin Effect and Interaction of Short Laser Pulses with Dense Plasmas." *Physical Review A*, vol. 42, no. 12, 1990, pp. 7401–7412.

[52] Fedosejevs, R., et al. "Absorption of Femtosecond Laser Pulses in High-Density Plasma." *Physical Review Letters*, vol. 64, no. 11, 1990, pp. 1250–1253.

Acknowledgements

At this point, I would like to thank each and every one who helped and supported me directly or indirectly, in the preparation and completion of this work.

I would like to thank Prof. Dr. Malte Kaluza for giving me the opportunity to work in his Relativistic Laser Physics group at the Institute of Optics and Quantum Electronics (IOQ), Jena. It was a great experience to work in the pleasant and constructive environment of POLARIS.

I would like to express my sincere gratitude to my advisor Dr. Sebastian Keppler for his continuous support and guidance throughout my time at IOQ. Thank you for the many discussions I had regarding the work and for making my time easy at POLARIS. I learned a lot from you.

I want to thank Issa Tamer for being there for any kind of discussions and help from the start when I started work at POLARIS. Thank you for the guidance in all matters and especially helping me at work in the compressor lab.

A big thanks to Dr. Marco Hornung and Marco Hellwing for helping me organize everything and being available to give their time to me whenever I required.

I would also like to mention Andreas with whom it was a pleasure to work and discuss science with. Thanks to Georg for the nice environment and jokes and to Matthew who shared his experience with interferometers with me.

I want to thank the entire POLARIS group and the RLP group for the nice working atmosphere.

A special thanks to my wife who has supported me through thick and thin, believed in me and encouraged me throughout these two years.

Thanks to my family (especially my parents) who have played an important role in making me come to Germany and have supported me through all my endeavors, dreams and decisions.